Journal of Applied Analysis and Computation
Volume 15, Number 2, April 2025, 705–733
Website:http://www.jaac-online.com
DOI:10.11948/20240098

BIFURCATION AND TURING PATTERN ANALYSIS FOR A SPATIOTEMPORAL DISCRETE DEPLETION TYPE GIERER-MEINHARDT MODEL WITH SELF-DIFFUSION AND CROSS-DIFFUSION

Yanhua Zhu[1], You Li[2], Xiangyi Ma[1], Ying Sun[1], Ziwei Wang[3] and Jinliang Wang[1,†]

Abstract This paper presents a study on spatiotemporal dynamics and Turing patterns in a space-time discrete depletion type Gierer-Meinhardt model with self-diffusion and cross-diffusion based on coupled map lattices (CMLs) model. Initially, the existence and stability conditions for fixed points are determined through linear stability analysis. Secondly, the conditions for the occurrence of flip bifurcation, Neimark–Sacker bifurcation, and Turing bifurcation are derived by means of the center manifold reduction theorem and bifurcation theory. The results indicate that there exist two nonlinear mechanisms, namely flip-Turing instability and Neimark–Sacker-Turing instability. Additionally, some numerical simulations are performed to illustrate the theoretical findings. Interestingly, a rich variety of dynamical behaviors, including period-doubling cascades, invariant circles, periodic windows, chaotic regions, and striking pattern formations (plaques, mosaics, curls, spirals, and other intermediate patterns), are observed. Finally, the evolution of pattern size and type is also simulated as the cross-diffusion coefficient varies. It reveals that cross-diffusion has a certain influence on the growth of patterns.

Keywords Space-time discrete systems, self-diffusion and cross-diffusion, pattern formation, Neimark-Sacker bifurcation, Gierer-Meinhardt model.

MSC(2010) 35B32, 35K57, 37G05.

1. Introduction

The reaction-diffusion equation is a mathematical model employed to depict the diffusion and reaction processes of substances in space. As a partial differential equation, it is commonly used to capture the variation of substance concentration or

[†]The corresponding author.
[1]Department of Mathematical Sciences, Beihang University, Beijing 100191, China
[2]Department of Sciences, Beijing Forestry University, Beijing 100083, China
[3]Department of Instrumentation and Optoelectronic Engineering, Beihang University, Beijing 100191, China
Email: zyh_jyo@163.com(Y. Zhu), liyou@bjfu.edu.cn(Y. Li), 15981923304@163.com(X. Ma), yings@buaa.edu.cn(Y. Sun), ziweiwang@buaa.edu.cn(Z. Wang), jlwang@buaa.edu.cn(J. Wang)

diffusion rate with respect to temporal and spatial. Turing mentioned in his previous research [38] that in reaction-diffusion systems, the diffusion term plays a crucial role in the formation of patterns. Additionally, he put forward the concept of Turing instability, which denotes the instability of the initially spatial homogeneous solution in reaction-diffusion systems due to the presence of the diffusion term. Currently, the application of Turing instability has expanded to a wide range of fields, including biology, physics, chemistry, embryogenesis, and various other domains [10, 12, 39, 42, 48–50]. As a widely applied model, the reaction-diffusion equation is frequently employed to characterize the diffusion and reaction behavior in the aforementioned diverse fields, thereby exhibiting various types of patterns, such as labyrinth, spot, gap, stripe, spiral and so on [1, 6, 20, 21, 40].

In order to describe the spatiotemporal pattern formation of tissue structures in embryology and regeneration, several types of reaction-diffusion equations in the form of molecular models, which include the activator-inhibitor type Gierer-Meinhardt system and the depletion type Gierer-Meinhardt (G-M) system, were proposed by Gierer and Meinhardt in [13]. To date, a significant number of scholars have carried out extensive research on the dynamical behavior of the activator-inhibitor type G-M system [19, 23, 26, 28, 36, 40–45, 47]. However, there is relatively little research on the depletion type G-M model, which can be represented in the following form:

$$\begin{cases} \dfrac{\partial a}{\partial t} = \varrho_0 \varrho + c\varrho a^k f(s) - \mu a + d_a \nabla^2 a, \\ \dfrac{\partial s}{\partial t} = c_0 - c' \varrho a^k f(s) - \nu s + d_s \nabla^2 s, \end{cases} \tag{1.1}$$

where $a(t,x,y)$ represents the activator concentration, and $s(t,x,y)$ stands for the concentration of the substrate. $f(s)$ is a function increasing with s, and the parameters ϱ_0, ϱ, c, k, μ, c_0, c', ν are all positive constants, for their specific biological significance, readers can refer to [13]. The Laplace operator is denoted by the symbol "∇^2" and $\nabla^2 = \frac{\partial^2}{\partial x^2} + \frac{\partial^2}{\partial y^2}$, d_a and d_s respectively represent the diffusion coefficients of self-diffusion for activator and substrate, respectively.

For generally function $f(s)$ and the positive constant k, it is challenging to determine the explicit expression for the equilibrium points of this system. Consequently, there remains substantial research potential in the field of the depletion type G-M model. In [13], the authors subsequently offered a simplified version of this system, which can be illustrated as follows:

$$\begin{cases} \dfrac{\partial a}{\partial t} = \varrho_0 \varrho + c\varrho a^2 s - \mu a + d_a \nabla^2 a, \\ \dfrac{\partial s}{\partial t} = c_0 - c' \varrho a^2 s - \nu s + d_s \nabla^2 s, \end{cases} \tag{1.2}$$

which corresponds to the scenario in system (1.1) where $k = 2$ and the function $f(s) = s$.

Based on [5, 29] and [16], the depletion type G-M model (1.2) are suitable for describing pigmentation patterns in sea shells and the ontogeny of ribbing on ammonoid shells. Nevertheless, the majority of the aforementioned studies predominantly consider the impact of self-diffusion on the system. In reality, the diffusion in nature involves cross-diffusion [17, 18, 37, 46], super-diffusion [4, 24, 25], and sub-diffusion [32], in addition to self-diffusion. Among these, cross-diffusion plays a significant role in revealing spatial and temporal complexity. According to the researches conducted in [17, 18, 37] and [46], it was observed that the cross-diffusion models generate more intricate and varied Turing patterns than their counterparts, which display comparatively less complex patterns through self-diffusion. Therefore, it is imperative to consider both self-diffusion and cross-diffusion simultaneously when studying chemical reaction models. Taking into account cross-diffusion, system (1.2) is transformed as follows:

$$\begin{cases} \dfrac{\partial a}{\partial t} = \varrho_0 \varrho + c\varrho a^2 s - \mu a + d_a \nabla^2 a + d_{\tilde{s}} \nabla^2 s, \\ \dfrac{\partial s}{\partial t} = c_0 - c^{'} \varrho a^2 s - \nu s + d_{\tilde{a}} \nabla^2 a + d_s \nabla^2 s, \end{cases} \tag{1.3}$$

here, $d_{\tilde{a}}$ and $d_{\tilde{s}}$ are the diffusion coefficients for cross-diffusion, respectively.

According to [13], ν is considered to be an insignificant amount, which can be neglected. Hence, it can be taken as 0. For convenience, we will nondimensionalize system (1.3). Let $a = \frac{c_0 c}{\mu c'} \bar{a}$, $s = \frac{\mu^2 c'}{c_0 c^2 \rho} \bar{s}$, $t = \frac{1}{\mu} \bar{t}$, $d_{11} = \frac{1}{\mu} d_a$, $d_{12} = \frac{\mu^2 c'^2}{c_0^2 c^3 \rho} d_{\hat{s}}$, $d_{21} = \frac{c_0^2 c^2 \rho}{\mu^4 c'^2} d_{\hat{a}}$, $d_{22} = \frac{1}{\mu} d_s$, $\sigma_{\bar{a}} = \frac{c_0 c \rho_0 \rho}{\mu^2 c'}$, $\sigma_{\bar{s}} = \frac{c_0^2 c^2 \rho}{\mu^3 c'}$. Then

$$\begin{cases} \dfrac{\partial \bar{a}}{\partial \bar{t}} = \bar{s}\bar{a}^2 - \bar{a} + \sigma_{\bar{a}} + d_{11} \nabla^2 \bar{a} + d_{12} \nabla^2 \bar{s}, \\ \dfrac{\partial \bar{s}}{\partial \bar{t}} = -\sigma_{\bar{s}} \bar{s}\bar{a}^2 + \sigma_{\bar{s}} + d_{21} \nabla^2 \bar{a} + d_{22} \nabla^2 \bar{s}. \end{cases} \tag{1.4}$$

For notational convenience, we will still use a, s, t, σ, μ instead of $\bar{a}$, $\bar{s}$, $\bar{t}$, $\sigma_{\bar{a}}$, $\sigma_{\bar{s}}$, respectively. System (1.4) now reads

$$\begin{cases} \dfrac{\partial a}{\partial t} = sa^2 - a + \sigma + d_{11} \nabla^2 a + d_{12} \nabla^2 s, \\ \dfrac{\partial s}{\partial t} = -\mu s a^2 + \mu + d_{21} \nabla^2 a + d_{22} \nabla^2 s. \end{cases} \tag{1.5}$$

It should be emphasized that the aforementioned research [23, 26, 36, 40–43, 45] carried out on G-M systems that are characterized by continuous temporally and spatially. In [28], the authors analyzed the dynamical beihavior of a G-M system that is characterized by temporally continuous but spatially discrete, commonly referred to as the dynamical behavior of a semi-discrete G-M system. In practice, when performing numerical simulations, it is essential to discretize the continuous system, thereby obtaining its discrete form, which inherently provides the algorithm for numerical simulations. Therefore, the discrete form acts as a natural bridge linking the actual model and its simulation. Furthermore, mathematical models are typically developed based on biological and chemical data, and observations and data collection are often performed at discrete time points and spatial locations. Consequently, this paper concentrates on the exploration of the depletion type G-M system within the context of discrete time and space.

When dealing with the spatiotemporal discretization of reaction-diffusion systems, the coupled map lattice (CMLs) method is frequently preferred. Researchers apply this method to the discrteization of various systems, including predator-prey systems [20], population models [11], and physical systems [34], leading to the derivation of corresponding CMLs model, which are subsequently investigated for their spatiotemporal dynamical behavior. The CMLs model preserves the inherent properties of the original system and exhibits superior advantages in capturing nonlinear characteristics and dynamic complexity when compared to continuous models. Notably, the patterns generated by the CMLs model are more varied and rich. Moreover, the CMLs model inherently captures an algorithmic representation, resulting in enhanced computational efficiency in numerical simulations utilizing this model. Consequently, the CMLs model provides a robust framework for describing and predicting pattern formation. Over the past few years, numerous studies focused on the dynamics of pattern formation have emerged by means of CMLs model, as exemplified by [20–22,27,35,41,51,52]. For more extensive investigations, please refer to [7,8,33].

Nevertheless, there is still a relatively limited amount of researches on the dynamics of CMLs model for G-M model, especially in the case of depletion model. In this paper, we explore the application of the CMLs model to the depletion type G-M model, leading to the development of a spatiotemporal discretized deleption type G-M model. By means of stability analysis and bifurcation analysis, we have discovered a variety of fascinating dynamical phenomena that cannot be extended to the corresponding continuous depletion G-M systems, including flip bifurcation and chaos. Turing patterns for the continuous depletion type G-M system can be induced by the mechanism of the destabilization of homogeneous steady state and the Hopf periodic solution due to the diffusion. However, in this paper, besides these mechanisms, we have uncovered additional mechanisms, including flip-Turing instability, Neimark-Sacker-Turing instability and chaotic oscillations, which can exhibit a variety of spatial patterns, such as plaques, mosaics, curls, spirals, and more. This enriches the study of pattern dynamics in G-M model.

The organization of this paper is outlined as follows. Section 2 introduces the CMLs model and presents a theoretical stability analysis. In Section 3, a detailed theoretical analysis of bifurcation, including flip, Neimark-Sacker, and Turing bifurcation, is conducted. Section 4 utilizes numerical simulations to illustrate the theoretical conclusions derived in Section 3 and showcases the observed dynamical behaviors and spatial patterns. Section 5 concludes the paper with a brief discussion and conclusion.

2. The CMLs model and stability analysis

In this section, we initially develop the CMLs model that corresponds to the continuous depletion type G-M model, and subsequently investigate its stability.

2.1. CMLs model of the depletion type G–M model

The depletion type G-M model to be examined in this paper is presented as system (1.5). We will investigate the dynamical behavior of the system (1.5) in two-dimensional space. The positions of a and s are represented by the spatial coordinates $r = (x, y)$.

By discretization of system (1.5), the CMLs model can be built as follows. In a two-dimensional rectangular region, we consider $n \times n$ lattices, and each lattice represents a site. Every site $(i, j), i, j \in \{1, 2, \cdots, n\}$ includes two numbers which are the density of activator $a(i, j, t)$ and the density of substrate $s(i, j, t)$ at time $t \in Z^+$. Assuming that there is a local reaction and spatial diffusion of activator and substrate at different sites [30,34], that is, the density of activator and substrate at each lattice varies with time following the system dynamics.

In the CMLs model, the dynamical behaviors of activator and substrate from t to $t+1$ consists of two stages: "reaction" stage and "diffusion" stage [20,30,34,35]. The diffusion behavior is observed prior to the reaction behavior. By taking into account the time step τ and space step δ and discretizing the spatial configuration of system (1.5), we are able to formulate the equations that govern the dispersal process:

$$a'(i,j,t) = a(i,j,t) + \frac{\tau}{\delta^2} d_{11} \nabla_d^2 a(i,j,t) + \frac{\tau}{\delta^2} d_{12} \nabla_d^2 s(i,j,t), \tag{2.1a}$$

$$s'(i,j,t) = s(i,j,t) + \frac{\tau}{\delta^2} d_{21} \nabla_d^2 a(i,j,t) + \frac{\tau}{\delta^2} d_{22} \nabla_d^2 s(i,j,t). \tag{2.1b}$$

The Laplacian operator ∇^2 in discrete form can be described by ∇_d^2:

$$\nabla_d^2 a(i,j,t) = a(i+1,j,t) + a(i-1,j,t) + a(i,j+1,t) + a(i,j-1,t) - 4a(i,j,t), \tag{2.2a}$$

$$\nabla_d^2 s(i,j,t) = s(i+1,j,t) + s(i-1,j,t) + s(i,j+1,t) + s(i,j-1,t) - 4s(i,j,t). \tag{2.2b}$$

According to [30], the discretization of the non-spatial form of (2.1) gives rise to the equations governing the reaction stage:

$$a(i,j,t+1) = f_1\left(a'(i,j,t), s'(i,j,t)\right), \tag{2.3a}$$

$$s(i,j,t+1) = g_1\left(a'(i,j,t), s'(i,j,t)\right), \tag{2.3b}$$

where

$$f_1(a,s) = a + \tau(sa^2 - a + \sigma), \tag{2.4a}$$

$$g_1(a,s) = s + \tau(-\mu s a^2 + \mu). \tag{2.4b}$$

Eqs. (2.1)–(2.4) represent the CMLs model of system (2.1). All the parameters in the CMLs model are positive and state variables $a(i,j,t)$ and $s(i,j,t)$ are non-negative. The periodic boundary conditions to the CMLs model are considered as following:

$$\begin{aligned} &a(i,0,t) = a(i,n,t),\ a(i,1,t) = a(i,n+1,t),\\ &a(0,j,t) = a(n,j,t),\ a(1,j,t) = a(n+1,j,t), \end{aligned} \tag{2.5a}$$

$$\begin{aligned} &s(i,0,t) = s(i,n,t),\ s(i,1,t) = s(i,n+1,t),\\ &s(0,j,t) = s(n,j,t),\ s(1,j,t) = s(n+1,j,t). \end{aligned} \tag{2.5b}$$

The dynamics of the discrete time and space depletion type G-M system have spatially homogeneous and heterogeneous dynamics. For all i, j, t, the homogeneous behavior satisfies

$$\nabla_d^2 a(i,j,t) = 0, \tag{2.6a}$$

$$\nabla_d^2 s(i,j,t) = 0. \tag{2.6b}$$

While for heterogeneous dynamics, there exists at least one group of i, j and t, such that $\nabla_d^2 a(i,j,t)$ and $\nabla_d^2 s(i,j,t)$ are non-zero.

According to the above analysis, the homogeneous dynamics can be determined by

$$a_{t+1} = a_t + \tau(s_t a_t^2 - a_t + \sigma), \tag{2.7a}$$

$$s_{t+1} = s_t + \tau(-\mu s_t a_t^2 + \mu). \tag{2.7b}$$

Subsequently, equation (2.7) can be redefined in the following mapping form:

$$\begin{pmatrix} a \\ s \end{pmatrix} \mapsto \begin{pmatrix} a + \tau\left(sa^2 - a + \sigma\right) \\ s + \tau(-\mu s a^2 + \mu) \end{pmatrix}. \tag{2.8}$$

As a consequence, when examining the homogeneous dynamics of the CMLs model (2.1)–(2.4), we can directly examine the map (2.8).

2.2. Analysis of the stability of the homogeneous steady state

Firstly, we obtain the fixed point of map (2.8) by solving the following equations (2.9):

$$\begin{cases} a = a + \tau\Big(sa^2 - a + \sigma\Big), \\ s = s + \tau\Big(-\mu s a^2 + \mu\Big). \end{cases} \tag{2.9}$$

Obviously, we can observe that (2.9) has a unique positive fixed point $(a_*, s_*) = \Big(1+\sigma, \frac{1}{(1+\sigma)^2}\Big)$. The corresponding Jacobian is depicted by

$$J(\tau) = \begin{pmatrix} 1 + \left(-1 + \dfrac{2}{1+\sigma}\right)\tau & (1+\sigma)^2\tau \\ -\dfrac{2\mu\tau}{1+\sigma} & 1 - \mu(1+\sigma)^2\tau \end{pmatrix}. \tag{2.10}$$

As described in [31], the fixed point is stable if the two eigenvalues of $J(\tau)$ satisfy $|\lambda_1| < 1$ and $|\lambda_2| < 1$. And if the two eigenvalues satisfy $|\lambda_1| > 1$ or $|\lambda_2| > 1$, the fixed point is unstable. The two eigenvalues of $J(\tau)$ are $\lambda_{1,2} = \frac{1}{2}\left(-p(\tau) \pm \sqrt{p^2(\tau) - 4q(\tau)}\right)$, where $p(\tau) = -TrJ(\tau)$, $q(\tau) = DetJ(\tau)$, $TrJ(\tau) = 2 - \frac{\left(-1+\sigma+\mu(1+\sigma)^3\right)\tau}{1+\sigma}$, and $DetJ(\tau) = \frac{1+\sigma-\left(-1+\sigma+\mu(1+\sigma)^3\right)\tau+\mu(1+\sigma)^3\tau^2}{1+\sigma}$.

Concerning the stability of fixed point (a_*, s_*), the following proposition presents a series of specific parameter conditions.

Proposition 2.1. *For the fixed point (a_*, s_*):*

(1) If one of conditions (H_1) and (H_2) is satisfied, it is a saddle, where

$$(H_1)\ \begin{cases} \sigma > 0, \\ \mu > \mu_1, \\ \tau_1 < \tau < \tau_2; \end{cases} \qquad (H_2)\ \begin{cases} \sigma > 1, \\ 0 < \mu < \mu_2, \\ \tau_1 < \tau < \tau_2; \end{cases}$$

(2) If one of conditions (SN_1) and (SN_2) is satisfied, it is a stable node, where

$$(SN_1)\ \begin{cases} \sigma > 0, \\ \mu > \mu_1, \\ 0 < \tau < \tau_1; \end{cases} \qquad (SN_2)\ \begin{cases} \sigma > 1, \\ 0 < \mu < \mu_2, \\ 0 < \tau < \tau_1; \end{cases}$$

And furthermore, if one of conditions (H_3) *and* (H_4) *is satisfied, it is a stable degenerate node, where*

$$(H_3)\quad \begin{cases} \sigma > 0, \\ \mu = \mu_1, \\ 0 < \tau < \tau_*; \end{cases} \qquad (H_4)\quad \begin{cases} \sigma > 1, \\ \mu = \mu_2, \\ 0 < \tau < \tau_*; \end{cases}$$

(3) If one of conditions (SF_1) *and* (SF_2) *is satisfied, it is a stable focus, where*

$$(SF_1)\quad \begin{cases} 0 < \sigma \leqslant 1, \\ \dfrac{1-\sigma}{(1+\sigma)^3} < \mu < \mu_1, \\ 0 < \tau < \tau_*; \end{cases} \qquad (SF_2)\quad \begin{cases} \sigma > 1, \\ \mu_2 < \mu < \mu_1, \\ 0 < \tau < \tau_*. \end{cases}$$

Among which, $\mu_1 = \frac{3+\sigma+\sqrt{8(1+\sigma)}}{(1+\sigma)^3}$, $\mu_2 = \frac{3+\sigma-\sqrt{8(1+\sigma)}}{(1+\sigma)^3}$, $\tau_* = 1 - \frac{1-\sigma}{\mu(1+\sigma)^3}$, $\tau_1 = \tau_* - \sqrt{\tau_*^2 - \frac{4}{\mu(1+\sigma)^2}}$, $\tau_2 = \tau_* + \sqrt{\tau_*^2 - \frac{4}{\mu(1+\sigma)^2}}$.

Proof. Direct computation. □

3. Bifurcation analysis of the homogeneous stationary state

In this section, we aims to analyze the flip bifurcation, Neimark-Sacker bifurcation, and Turing bifurcation of system (2.1), with τ serving as the main bifurcation parameter. Additionally, we will examine how parameter τ affects the dynamical behaviors of the system.

3.1. Flip bifurcation

The loss of stability of the fixed point and the emergence of a flip bifurcation result in the bifurcation of period-2 points from the fixed point. The occurrence of flip bifurcation necessitates that one of the eigenvalues of $J(\tau)$ is equal to -1, while the absolute value of the other eigenvalue is not equal to 1 at the critical value. To satisfy these two requirements, the bifurcation parameter must meet the following conditions:

$$\begin{cases} \sigma > 0, \\ \mu > \mu_1, \\ \tau = \tau_1, \\ \tau \neq \dfrac{2(1+\sigma)}{(-1+\sigma+\mu(1+\sigma)^3)} \ or\ \dfrac{4(1+\sigma)}{(-1+\sigma+\mu(1+\sigma)^3)}; \end{cases}$$

$$\begin{cases} \sigma > 1, \\ 0 < \mu < \mu_2, \\ \tau = \tau_1, \\ \tau \neq \dfrac{2(1+\sigma)}{(-1+\sigma+\mu(1+\sigma)^3)} \ or\ \dfrac{4(1+\sigma)}{(-1+\sigma+\mu(1+\sigma)^3)}; \end{cases}$$

After a simple analysis, when $\tau = \tau_1$, $\tau \neq \frac{2(1+\sigma)}{(-1+\sigma+\mu(1+\sigma)^3)}$ is equal to $\mu \neq 0$, $\tau \neq \frac{4(1+\sigma)}{(-1+\sigma+\mu(1+\sigma)^3)}$ is equal to $\mu \neq \mu_1$ or μ_2. Therefore, the above two conditions can be simplified to the following conditions (SN_3) and (SN_4):

$$(SN_3)\begin{cases}\sigma > 0,\\ \mu > \mu_1,\\ \tau = \tau_1;\end{cases} \qquad (SN_4)\begin{cases}\sigma > 1,\\ 0 < \mu < \mu_2,\\ \tau = \tau_1;\end{cases}$$

The center manifold theorem plays a significant role in determining the stability of the bifurcated periodic-2 points. Next, the maps (2.8) is reduced by means of the center manifold theorem. To achieve this, taking τ as an independent variable and let $w = a - a_*$, $z = s - s_*$, and $\tilde{\tau} = \tau - \tau_1$, then map (2.8) is transformed into the following form:

$$\begin{pmatrix} w \\ z \\ \tilde{\tau} \end{pmatrix} = \begin{pmatrix} a_{100} & a_{010} & 0 \\ b_{100} & b_{010} & 0 \\ 0 & 0 & 1 \end{pmatrix} \begin{pmatrix} w \\ z \\ \tilde{\tau} \end{pmatrix} + \begin{pmatrix} f_1(w,z,\tilde{\tau}) \\ f_2(w,z,\tilde{\tau}) \\ f_3(w,z,\tilde{\tau}) \end{pmatrix} \tag{3.1}$$

where

$$\begin{aligned} f_1(w,z,\tilde{\tau}) =& a_{200}w^2 + a_{110}wz + a_{101}w\tilde{\tau} + a_{011}z\tilde{\tau} \\ & + a_{210}w^2 z + a_{201}w^2\tilde{\tau} + a_{111}wz\tilde{\tau} + O(4), \\ f_2(w,z,\tilde{\tau}) =& b_{200}w^2 + b_{110}wz + b_{101}w\tilde{\tau} + b_{011}z\tilde{\tau} \\ & + b_{210}w^2 z + b_{201}w^2\tilde{\tau} + b_{111}wz\tilde{\tau} + O(4), \\ f_3(w,z,\tilde{\tau}) =& 0, \end{aligned}$$

among them, $a_{100} = 1 + \left(-1 + \frac{2}{1+\sigma}\right)\tau_1$, $a_{010} = (1+\sigma)^2\tau_1$, $b_{100} = -\frac{2\mu\tau_1}{1+\sigma}$, $b_{010} = 1 - \mu(1+\sigma)^2\tau_1$, $a_{200} = \frac{\tau_1}{(1+\sigma)^2}$, $a_{110} = 2(1+\sigma)\tau_1$, $a_{101} = \frac{1-\sigma}{1+\sigma}$, $a_{011} = (1+\sigma)^2$, $a_{210} = \tau_1$, $a_{201} = \frac{1}{(1+\sigma)^2}$, $a_{111} = 2(1+\sigma)$; $b_{200} = -\frac{\mu\tau_1}{(1+\sigma)^2}$, $b_{110} = -2\mu(1+\sigma)\tau_1$, $b_{101} = -\frac{2\mu}{1+\sigma}$, $b_{011} = -\mu(1+\sigma)^2$, $b_{210} = -\mu\tau_1$, $b_{201} = -\frac{\mu}{(1+\sigma)^2}$, $b_{111} = -2\mu(1+\sigma)$, and $O(4)$ represents a polynomial term in the variables (w, z, τ) of the order equal to or great than 4.

Subsequently, carrying out the inverse transformation $w = a_{020}(\tilde{w} + \tilde{z})$ and $z = (-1 - a_{100})\tilde{w} + (\lambda_2 - a_{100})\tilde{z}$ with $\lambda_2 = 1 + a_{100} + b_{010}$, system (3.1) is able to be converted to the following format:

$$\begin{aligned} \tilde{w} &\mapsto -\tilde{w} + \frac{1}{a_{010}\,(1+\lambda_2)} F_1(\tilde{w}, \tilde{z}, \tilde{\tau}), \\ \tilde{z} &\mapsto \lambda_2 \tilde{z} + \frac{1}{a_{010}\,(1+\lambda_2)} F_2(\tilde{w}, \tilde{z}, \tilde{\tau}), \\ \tilde{\tau} &\mapsto \tilde{\tau}, \end{aligned} \tag{3.2}$$

here

$$\begin{aligned} & F_1(\tilde{w}, \tilde{z}, \tilde{\tau}) \\ =& a_{010}[(\lambda_2 - a_{100})\,a_{101} - a_{010}b_{101}](\tilde{w} + \tilde{z})\tilde{\tau} + a_{010}^2[a_{200}\,(\lambda_2 - a_{100}) - a_{010}b_{200}] \end{aligned}$$

$$
\begin{aligned}
&\times(\tilde{w}+\tilde{z})^2+a_{010}[(\lambda_2-a_{100})\,a_{110}-a_{010}b_{110}][\tilde{w}\,(-1-a_{100})+\tilde{z}\,(\lambda_2-a_{100})]\\
&\times(\tilde{w}+\tilde{z})+a_{010}[(\lambda_2-a_{100})\,a_{111}-a_{010}b_{111}][\tilde{w}\,(-1-a_{100})+\tilde{z}\,(\lambda_2-a_{100})]\\
&\times(\tilde{w}+\tilde{z})\tilde{\tau}+a_{010}^2[(\lambda_2-a_{100})\,a_{210}-a_{010}b_{210}][\tilde{w}\,(-1-a_{100})+\tilde{z}\,(\lambda_2-a_{100})]\\
&\times(\tilde{w}+\tilde{z})^2+[(\lambda_2-a_{100})\,a_{011}-a_{010}b_{011}][\tilde{w}\,(-1-a_{100})+\tilde{z}\,(\lambda_2-a_{100})]\tilde{\tau}\\
&+a_{010}^2[(\lambda_2-a_{100})\,a_{201}-a_{010}b_{201}](\tilde{w}+\tilde{z})^2\tilde{\tau}+O(4),
\end{aligned}
$$

and

$$
\begin{aligned}
&F_2(\tilde{w},\tilde{z},\tilde{\tau})\\
=&a_{010}[(1+a_{100})\,a_{101}+a_{010}b_{101}](\tilde{w}+\tilde{z})\tilde{\tau}+a_{010}^2[(1+a_{100})\,a_{200}+a_{010}b_{200}](\tilde{w}+\tilde{z})^2\\
&+a_{010}[(1+a_{100})\,a_{110}+a_{010}b_{110}][\tilde{w}\,(-1-a_{100})+\tilde{z}\,(-a_{100}+\lambda_2)](\tilde{w}+\tilde{z})\\
&+a_{010}[(1+a_{100})\,a_{111}+a_{010}b_{111}][\tilde{w}\,(-1-a_{100})+\tilde{z}\,(-a_{100}+\lambda_2)](\tilde{w}+\tilde{z})\tilde{\tau}\\
&+a_{010}^2[(1+a_{100})\,a_{210}+a_{010}b_{210}][\tilde{w}\,(-1-a_{100})+\tilde{z}\,(-a_{100}+\lambda_2)](\tilde{w}+\tilde{z})^2\\
&+[(1+a_{100})\,a_{011}+a_{010}b_{011}][\tilde{w}\,(-1-a_{100})+\tilde{z}\,(-a_{100}+\lambda_2)]\tilde{\tau}\\
&+a_{010}^2[(1+a_{100})\,a_{201}+a_{010}b_{201}](\tilde{w}+\tilde{z})^2\tilde{\tau}+O(4).
\end{aligned}
$$

In order to ascertain pertinent information about the stability of the bifurcated period-2 orbit, it is imperative to formulate the governing equation that dependent on the center manifold. We proceed under the assumption that the center manifold is given by the following representation:

$$
W^c(0,0,0)=\left\{(\tilde{w},\tilde{z},\tilde{\tau})\in R^3 \mid \tilde{z}=h^*(\tilde{w},\tilde{\tau}),\ h^*(0,0)=0,\ Dh^*(0,0)=0\right\}, \quad (3.3)
$$

where $h^*(\tilde{w},\tilde{\tau})=e_1\tilde{w}^2+e_2\tilde{w}\tilde{\tau}+e_3\tilde{\tau}^2+O(3)$. Taking $\tilde{z}=h^*(\tilde{w},\tilde{\tau})$ into map (3.1), it is possible for us to achieve

$$
\begin{aligned}
\lambda_2 h^*(w,\tilde{\tau})+\frac{F_2(\tilde{w},h^*(\tilde{w},\tilde{\tau}),\tilde{\tau})}{a_{010}(1+\lambda_2)}=&e_1\left[-\tilde{w}+\frac{F_1(\tilde{w},h^*(\tilde{w},\tilde{\tau}),\tilde{\tau})}{a_{010}(1+\lambda_2)}\right]^2\\
&+e_2\left[-\tilde{w}+\frac{F_1(\tilde{w},h^*(\tilde{w},\tilde{\tau}),\tau)}{a_{010}(1+\lambda_2)}\right]\tilde{\tau}+e_3\tilde{\tau}^2+O(3).
\end{aligned} \quad (3.4)
$$

By comparing the terms $\tilde{w}^2, \tilde{w}\tilde{\tau}, \tilde{\tau}^2$, we can attain

$$
\begin{aligned}
e_1=&\frac{(1+a_{100})^2\,a_{110}-a_{010}\left((1+a_{100})\,a_{200}-(1+a_{100})\,b_{110}+a_{010}b_{200}\right)}{-1+\lambda_2^2},\\
e_2=&\frac{a_{011}\,(1+a_{100})^2-a_{010}\left((1+a_{100})\,a_{101}-(1+a_{100})\,b_{011}+a_{010}b_{101}\right)}{a_{010}\,(1+\lambda_2)^2},\\
e_3=&0.
\end{aligned} \quad (3.5)
$$

Correspondingly, by restricting map (3.1) to the center manifold, one can derive

$$
\tilde{w}\mapsto -\tilde{w}+\mu_1\tilde{w}^2+\mu_2\tilde{w}\tilde{\tau}+\mu_3\tilde{w}^2\tilde{\tau}+\mu_4\tilde{w}\tilde{\tau}^2+\mu_5\tilde{w}^3+O(4), \quad (3.6)
$$

here

$$
\mu_1=\frac{a_{100}^2a_{110}+a_{100}\left(a_{010}\left(-a_{200}+b_{110}\right)-a_{110}\left(-1+\lambda_2\right)\right)-a_{110}\lambda_2)}{1+\lambda_2}
$$

$$+ \frac{a_{010}\left(b_{110} - a_{010}b_{200} + a_{200}\lambda_2\right)}{1+\lambda_2},$$

$$\mu_2 = \frac{a_{011}\left(1+a_{100}\right)\left(a_{100}-\lambda_2\right) + a_{010}\left(b_{11} + a_{100}\left(b_{011}-a_{101}\right) - a_{010}b_{101} + a_{101}\lambda_2\right)}{a_{010}\left(1+\lambda_2\right)},$$

$$\mu_3 = \frac{1}{a_{010}\left(1+\lambda_2\right)}\Big(\left[-a_{010}\left(a_{010}b_{101} + \left(a_{101} - b_{011}\right)\left(a_{100} - \lambda_2\right)\right) + a_{011}\left(a_{100} - \lambda_2\right)^2\right]$$
$$\times e_1 + \left[a_{010}\left(2a_{100}^2 a_{110} - 2a_{010}^2 b_{200} + a_{100}\left(2a_{010}\left(b_{110} - a_{200}\right) + a_{110}\left(1-3\lambda_2\right)\right)\right.\right.$$
$$\left. + \; a_{110}\left(\lambda_2 - 1\right)\lambda_2 + a_{010}\left(2a_{200}\lambda_2 - b_{110}\left(\lambda_2-1\right)\right)\right)\Big] e_2 + a_{010}\Big[a_{111}\left(a_{100}^2 - \lambda_2\right)$$
$$+ a_{100}\left(a_{010}\left(b_{111} - a_{201}\right) - a_{111}\left(\lambda_2 - 1\right)\right) + a_{010}\left(b_{111} - a_{010}b_{201} + a_{201}\lambda_2\right)\Big]\Big),$$

$$\mu_4 = \frac{e_2\left(-a_{010}\left(a_{010}b_{101} + \left(a_{101} - b_{011}\right)\left(a_{100} - \lambda_2\right)\right) + a_{011}\left(a_{100} - \lambda_2\right)^2\right)}{a_{010}\left(1+\lambda_2\right)},$$

$$\mu_5 = \frac{1}{\left(1+\lambda_2\right)}\Big(\big[2a_{100}^2 a_{110} - 2a_{010}^2 b_{200} + a_{100}\left(2a_{010}\left(-a_{200} + b_{110}\right) + a_{110}\left(1-3\lambda_2\right)\right)$$
$$+ a_{110}\left(\lambda_2 - 1\right)\lambda_2 + a_{010}\left(-b_{110}\left(\lambda_2 - 1\right) + 2a_{200}\lambda_2\right)\big] e_1 + a_{010}\left(1+a_{100}\right)$$
$$\times \left(a_{100}a_{210} + a_{010}b_{210} - a_{210}\lambda_2\right)\Big).$$

As stated by the flip bifurcation theorem in [15], the emergence of flip bifurcation for map (3.6) requires

$$\eta_1 = \left.\left(\frac{\partial^2 F}{\partial\tilde{w}\partial\tilde{\tau}} + \frac{1}{2}\frac{\partial F}{\partial\tilde{\tau}}\cdot\frac{\partial^2 F}{\partial\tilde{w}^2}\right)\right|_{(\tilde{w},\tilde{\tau})=(0,0)} = \mu_2 \neq 0,$$

$$\eta_2 = \left.\left(\frac{1}{6}\frac{\partial^3 F}{\partial w^3} + \left(\frac{1}{2}\frac{\partial^2 F}{\partial\tilde{w}^2}\right)^2\right)\right|_{(\tilde{w},\tilde{\tau})=(0,0)} = \mu_5 + \mu_1^2 \neq 0.$$

After examining the aforementioned analysis, the following conclusion can be derived.

Theorem 3.1. *The map (2.8) undergoes a flip bifurcation at* (a_*, s_*), *if* (SN_3) *or* (SN_4) *satisfies and* $\eta_1 \neq 0, \eta_2 \neq 0$. *Moreover, if* $\eta_2 > 0$, *the stable periodic–2 points bifurcate from* (a_*, s_*); *and if* $\eta_2 < 0$, *the unstable periodic–2 points bifurcate from* (a_*, s_*).

Remark 3.1. In reality, the sign of η_2 is variable. Let's illustrate this fact with an example. We choose the range of μ to be $(0.003, 0.005)$ and the range of σ to be $(5.5, 6)$, and then simulate their relationship as shown in Figure 1. By observing Figure 1, we can see that the surface can be positive or negative, which means that as μ and σ vary, η_2 is a quantity with a changing sign.

3.2. Neimark-Sacker bifurcation

As stated by [15], when a fixed point undergoes Neimark-Sacker bifurcation, an invariant cycle surrounding the fixed point is created. The occurrence of this bifurcation necessitates the following conditions: there must be a pair of conjugate complex eigenvalues for the Jacobian matrix (2.9); furthermore, both eigenvalues

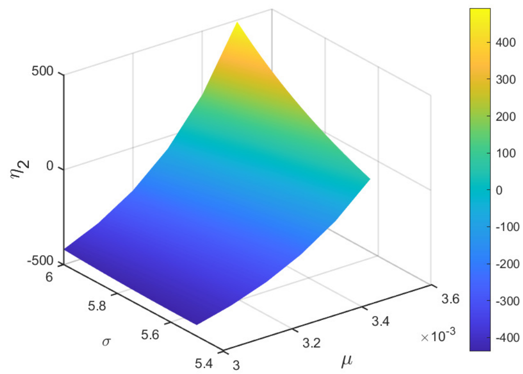

Figure 1. The flip bifurcation surface in parameter space (μ, σ, η_2).

must have a modulus of 1, which means $p(\tau)^2 - 4q(\tau) < 0$ and $q(\tau) = 1$, namely

$$\begin{cases} \sigma > 0, \\ \mu_2 < \mu < \mu_1, \\ \tau = \tau_*. \end{cases} \tag{3.7}$$

Additionally, the Neimark-Sacker bifurcation theorem [15] mandates that the transversality condition should not be zero, according to direct computations, it can be observed that

$$\frac{d|\lambda(\tau_*)|}{d\tau} = \frac{-1 + \sigma + \mu(1+\sigma)^3}{2(1+\sigma)} > 0. \tag{3.8}$$

Moreover, the Neimark-Sacker bifurcation demands

$$(\lambda(\tau_*))^\theta \neq 1, \quad \theta = 1, 2, 3, 4, \tag{3.9}$$

which means

$$\mu \neq \frac{2}{(1+\sigma)^3} \pm \sqrt{\frac{3-\sigma}{(1+\sigma)^5}} \; or \; \frac{5+\sigma}{2(1+\sigma)^3} \pm \frac{\sqrt{3}}{2}\sqrt{\frac{7-\sigma}{(1+\sigma)^5}}. \tag{3.10}$$

It is can be shown that $\frac{2}{(1+\sigma)^3} \pm \sqrt{\frac{3-\sigma}{(1+\sigma)^5}}$ and $\frac{5+\sigma}{2(1+\sigma)^3} \pm \frac{\sqrt{3}}{2}\sqrt{\frac{7-\sigma}{(1+\sigma)^5}}$ belong to (μ_1, μ_2). The transformation $w = a - a_*, z = s - s_*$ is utilized to shift the fixed point (a_*, s_*) to the origin $(0, 0)$, which simplifies the subsequent description and analysis. In light of this coordinate transformation, map (2.7) can be represented as follows:

$$\begin{pmatrix} w \\ z \end{pmatrix} \mapsto \begin{pmatrix} a_{10} & a_{01} \\ b_{10} & b_{01} \end{pmatrix} \begin{pmatrix} w \\ z \end{pmatrix} + \begin{pmatrix} a_{20}w^2 + a_{11}wz + a_{21}w^2z + a_{30}w^3 + \mathcal{O}(4) \\ b_{20}w^2 + b_{11}wz + b_{21}w^2z + b_{30}w^3 + \mathcal{O}(4) \end{pmatrix}, \tag{3.11}$$

where $a_{10} = 1 + \frac{(1-\sigma)\tau_*}{1+\sigma}$, $a_{01} = (1+\sigma)^2\tau_*$, $a_{20} = \frac{\tau_*}{(1+\sigma)^2}$, $a_{11} = 2(1+\sigma)\tau_*$, $a_{21} = \tau_*$, $a_{30} = 0$, $b_{10} = -\frac{2\mu\tau_*}{1+\sigma}$, $b_{01} = 1 - \mu(1+\sigma)^2\tau_*$, $b_{20} = \frac{-\mu\tau_*}{(1+\sigma)^2}$, $b_{11} = -2\mu(1+\sigma)\tau_*$,

$b_{21} = -\mu\tau_*$, $b_{30} = 0$. The corresponding two eigenvalues are

$$\lambda(\tau_*), \bar{\lambda}(\tau_*) = \frac{\mathrm{tr}J(\tau_*)}{2} \pm \frac{\mathrm{i}}{2}\sqrt{4\mathrm{Det}J(\tau_*) - \mathrm{tr}J(\tau_*)^2} := \alpha \pm \mathrm{i}\beta,$$

where $J(\tau_*) = J(a_*, s_*)|_{\tau=\tau_*}$, $\mathrm{i}^2 = -1$ and $|\lambda(\tau_*)| = |\bar{\lambda}(\tau_*)| = 1$.

With a view to exploring the Neimark-Sacker bifurcation, we need to derive the normal form of map (3.11) by means of center manifold reduction so as to meet the final requirement. Assume

$$\begin{pmatrix} w \\ z \end{pmatrix} = \begin{pmatrix} a_{01} & 0 \\ \alpha - a_{10} & -\beta \end{pmatrix} \begin{pmatrix} \tilde{w} \\ \tilde{z} \end{pmatrix}. \tag{3.12}$$

Afterwards, we can obtain

$$\begin{aligned} \tilde{w} &\mapsto \alpha\tilde{w} - \beta\tilde{z} + \frac{1}{a_{01}\beta}G_1(\tilde{w}, \tilde{z}), \\ \tilde{z} &\mapsto \beta\tilde{w} + \alpha\tilde{z} + \frac{1}{a_{01}\beta}G_2(\tilde{w}, \tilde{z}), \end{aligned} \tag{3.13}$$

here

$$\begin{aligned} G_1(\tilde{w}, \tilde{z}) = &- a_{21}a_{01}^2\beta^2\tilde{w}^2\tilde{z} + [(\alpha - a_{10})a_{11} + a_{01}a_{20}]\, a_{01}\beta\tilde{w}^2 - a_{11}a_{01}\beta^2\tilde{w}\tilde{z} \\ &+ (\alpha - a_{10})a_{21}a_{01}^2\beta\tilde{w}^3 + O(4), \\ G_2(\tilde{w}, \tilde{z}) = &\left[(\alpha - a_{10})^2 a_{11} - a_{01}\left((a_{10} - \alpha)\, a_{20} + (\alpha - a_{10})\, b_{11} + a_{01}b_{20}\right)\right] a_{01}\tilde{w}^2 \\ &+ [(a_{10} - \alpha)\, a_{11} + a_{01}b_{11}]\, a_{01}\beta\tilde{w}\tilde{z} - [(\alpha - a_{10})\left((a_{10} - \alpha)a_{21} + a_{01}b_{21}\right)] \\ &\times a_{01}^2\tilde{w}^3 + [(a_{10} - \alpha)a_{21} + a_{01}b_{21}]\, a_{01}^2\beta\tilde{w}^2\tilde{z} + O(4). \end{aligned} \tag{3.14}$$

In order to ensure the Neimark–Sacker bifurcation for map (3.13) occurs, we demand the determinative quantity κ satisfying

$$\kappa = -\mathrm{Re}\left(\frac{(1-2\lambda)\bar{\lambda}^2}{1-\lambda}\xi_{11}\xi_{20}\right) - \frac{1}{2}|\xi_{11}|^2 - |\xi_{02}|^2 + \mathrm{Re}(\bar{\lambda}\xi_{21}) \neq 0, \tag{3.15}$$

where

$$\begin{aligned} \xi_{20} &= \frac{1}{8a_{01}\beta}\Big[G_{1\tilde{w}\tilde{w}} - G_{1\tilde{z}\tilde{z}} + 2G_{2\tilde{w}\tilde{z}} + \mathrm{i}(G_{2\tilde{w}\tilde{w}} - G_{2\tilde{z}\tilde{z}} - 2G_{1\tilde{w}\tilde{z}})\Big], \\ \xi_{11} &= \frac{1}{4a_{01}\beta}\Big[G_{1\tilde{w}\tilde{w}} + G_{1\tilde{z}\tilde{z}} + \mathrm{i}(G_{2\tilde{w}\tilde{w}} + G_{2\tilde{z}\tilde{z}})\Big], \\ \xi_{02} &= \frac{1}{8a_{01}\beta}\left[G_{1\tilde{w}\tilde{w}} - G_{1\tilde{z}\tilde{z}} - 2G_{2\tilde{w}\tilde{z}} + \mathrm{i}(G_{2\tilde{w}\tilde{w}} - G_{2\tilde{z}\tilde{z}} + 2G_{1\tilde{w}\tilde{z}})\right], \\ \xi_{21} &= \frac{1}{16a_{01}\beta}\left[G_{1\tilde{w}\tilde{w}\tilde{w}} + G_{1\tilde{w}\tilde{z}\tilde{z}} + G_{2\tilde{w}\tilde{w}\tilde{z}} + G_{2\tilde{z}\tilde{z}\tilde{z}}\right. \\ &\qquad \left. + \mathrm{i}(G_{2\tilde{w}\tilde{w}\tilde{w}} + G_{2\tilde{w}\tilde{z}\tilde{z}} - G_{1\tilde{w}\tilde{w}\tilde{z}} - G_{1\tilde{z}\tilde{z}\tilde{z}})\right], \end{aligned}$$

with
$G_{1\tilde{w}\tilde{w}} = \beta a_{01}\,(2\,(\alpha - a_{10})\, a_{11} + 2a_{01}a_{20})$, $G_{1\tilde{w}\tilde{z}} = -\beta^2 a_{01}a_{11}$, $G_{1\tilde{z}\tilde{z}} = 0$, $G_{1\tilde{z}\tilde{z}\tilde{z}} = 0$, $G_{2\tilde{w}\tilde{w}} = 2a_{01}\left((\alpha - a_{10})^2 a_{11} - a_{01}\left((a_{10} - \alpha)\, a_{20} + (\alpha - a_{10})\, b_{11} + a_{01}b_{20}\right)\right)$, $G_{2\tilde{w}\tilde{z}} =$

$\beta a_{01}\left((a_{10}-\alpha)\,a_{11}+a_{01}b_{11}\right)$, $G_{2\tilde{z}\tilde{z}}=0$, $G_{1\tilde{w}\tilde{w}\tilde{w}}=6\beta a_{01}^2\left(\alpha-a_{10}\right)a_{21}$, $G_{1\tilde{w}\tilde{z}\tilde{z}}=0$, $G_{2\tilde{w}\tilde{w}\tilde{z}}=2\beta a_{01}^2\left((a_{10}-\alpha)a_{21}+a_{01}b_{21}\right)$, $G_{2\tilde{z}\tilde{z}\tilde{z}}=0$, $G_{2\tilde{w}\tilde{z}\tilde{z}}=0$, $G_{2\tilde{w}\tilde{w}\tilde{w}}=-6a_{01}^2\left(\alpha-a_{10}\right)\left((a_{10}-\alpha)\,a_{21}+a_{01}b_{21}\right)$, $G_{1\tilde{w}\tilde{w}\tilde{z}}=-2\beta^2a_{01}^2a_{21}$, which are the second and third order partial derivatives of $G_1(a_*,s_*)$ and $G_2(a_*,s_*)$ at $(0,0)$. Through the aforementioned discussion, (3.15) can be restated in the following form:

$$\kappa=-\frac{G_{1\tilde{w}\tilde{w}}(\omega\phi-\rho\varphi)-G_{2\tilde{w}\tilde{w}}(\omega\varphi+\rho\phi)}{32(a_{01}\beta)^2(1-\alpha^2+\beta^2)}-\frac{G_{1\tilde{w}\tilde{w}}^2+G_{2\tilde{w}\tilde{w}}^2}{32(a_{01}^2\beta)^2}-\frac{\epsilon^2+\varepsilon^2}{64(a_{01}^2\beta)^2}+\frac{\alpha\chi+\beta\gamma}{16a_{01}\beta},\tag{3.16}$$

where
$\omega=G_{1\tilde{w}\tilde{w}}+2G_{2\tilde{w}\tilde{z}}$, $\rho=G_{2\tilde{w}\tilde{w}}-2G_{1\tilde{w}\tilde{z}}$, $\epsilon=(G_{1\tilde{w}\tilde{w}}-2G_{2\tilde{w}\tilde{z}})^2$,
$\varepsilon=(G_{2\tilde{w}\tilde{w}}+2G_{1\tilde{w}\tilde{z}})^2$, $\chi=(G_{1\tilde{w}\tilde{w}\tilde{w}}+G_{2\tilde{w}\tilde{w}\tilde{z}})$, $\gamma=(G_{2\tilde{w}\tilde{w}\tilde{w}}-G_{1\tilde{w}\tilde{w}\tilde{z}})$,
$\phi=2\alpha^4-2\beta^4-6\alpha^3\beta-3\alpha^3+2\alpha\beta^2+\alpha^2+\beta^2$, $\varphi=2\alpha^3\beta+4\alpha\beta^3+5\alpha^2\beta+\beta^3-2\alpha\beta$.

Taking into account the above analysis, we can arrive at the following theorem:

Theorem 3.2. *Assume $\mu_2<\mu<\mu_1$ and condition (3.10) holds. If $\kappa\neq 0$, then map (2.8) undergoes Neimark–Sacker bifurcation at the fixed point (a_*,s_*) when $\tau=\tau_*$. In addition, if $\kappa<0$, an attracting invariant circle will occur when $\tau>\tau_*$; and if $\kappa>0$, an repelling invariant circle will occur when $\tau<\tau_*$.*

Remark 3.2. In fact, κ is also a quantity with sign change. Selecting the range of μ is $(0.0183, 0.02)$, and taking the range of σ is $(0.9035, 0.905)$, we simulate the relationship of κ, μ and σ in parameter space (μ,σ,κ), which are presented in Figure 2. By examining Figure 2, we observe that the surface can be either positive or negative, which implies that as μ and σ change, κ is a quantity with a changing sign.

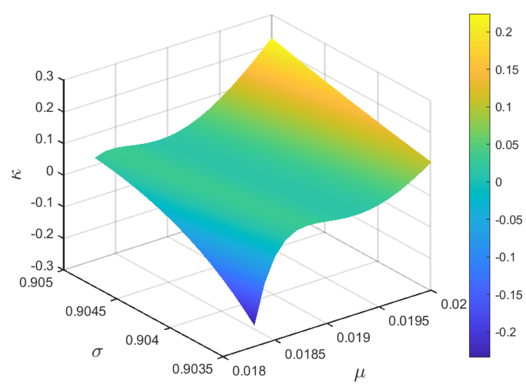

Figure 2. The Neimark-Sacker bifurcation surface in parameter space (μ,σ,κ).

3.3. Turing bifurcation

Spatial symmetry breaking is the main factor behind Turing bifurcation. If Turing instability takes place, the stable homogeneous stationary state of the CMLs model is driven to become unstable due to disparities in spatial diffusion, resulting in spatial pattern formation. For Turing bifurcation to happen, two prerequisites are essential [1, 9, 20]. Firstly, a nontrivial homogeneous stationary state must be temporally steady. Secondly, a e stable nontrivial homogeneous stationary state must become unstable under one or more kinds of spatially varied perturbations. According to Proposition 1, if any of conditions (SN_1)–(SN_2), (H_3)–(H_4) and (SF_1)–(SF_2) are fulfilled, then (a_*, s_*) will remain stable over time. In this section, we assume that one of (SN_1)–(SN_2), (H_3)–(H_4) and (SF_1)–(SF_2) is valid, and investigate the Turing bifurcation of the homogeneous steady state.

To ascertain the conditions that lead to Turing instability, we initially address the eigenvalue issues associated with the discrete Laplacian operator ∇_d^2. Given a discrete Laplacian operator ∇_d^2, its eigenvalue λ can be obtained by solving the following equation:

$$\nabla_d^2 X^{ij} + \lambda X^{ij} = 0, \tag{3.17}$$

and satisfy the following periodic boundary conditions:

$$X^{i,0} = X^{i,n},\ X^{i,1} = X^{i,n+1},\ X^{0,j} = X^{n,j},\ X^{1,j} = X^{n+1,j}, \tag{3.18}$$

Similarly, as mentioned in [2], the eigenvalues of the discrete Laplacian operator ∇_d^2 are:

$$\lambda_{kl} = 4\left(\sin^2\left(\frac{(k-1)\pi}{n}\right) + \sin^2\left(\frac{(l-1)\pi}{n}\right)\right),\ l, k \in \{1, 2, \cdots, n\}. \tag{3.19}$$

For the purpose of analyzing the Turing bifurcation, a spatially inhomogeneous perturbation is applied at the spatially uniform steady state (a_*, s_*). The equation for the spatially inhomogeneous perturbation can be expressed as:

$$\tilde{a}_{(i,j,t)} = a_{(i,j,t)} - a_*, \tilde{s}_{(i,j,t)} = s_{(i,j,t)} - s_*, \tag{3.20}$$

note that $\nabla_d^2 \tilde{a}_{(i,j,t)} = \nabla_d^2 a_{(i,j,t)}, \nabla_d^2 \tilde{s}_{(i,j,t)} = \nabla_d^2 s_{(i,j,t)}$, and the values of the two are not always zero.

Inserting the above disturbance equation into the CMLs model equation yields:

$$\begin{aligned}\tilde{a}_{(i,j,t+1)} =& a_{10}(\tilde{a}_{(i,j,t)} + \frac{\tau}{\delta^2} d_{11} \nabla_d^2 \tilde{a}_{(i,j,t)} + \frac{\tau}{\delta^2} d_{12} \nabla_d^2 \tilde{s}_{(i,j,t)}) \\ &+ a_{01}(\tilde{s}_{(i,j,t)} + \frac{\tau}{\delta^2} d_{21} \nabla_d^2 \tilde{a}_{(i,j,t)} + \frac{\tau}{\delta^2} d_{22} \nabla_d^2 \tilde{s}_{(i,j,t)}) + O(2), \qquad (3.21a)\\ \tilde{s}_{(i,j,t+1)} =& b_{10}(\tilde{a}_{(i,j,t)} + \frac{\tau}{\delta^2} d_{11} \nabla_d^2 \tilde{a}_{(i,j,t)} + \frac{\tau}{\delta^2} d_{12} \nabla_d^2 \tilde{s}_{(i,j,t)}) \\ &+ b_{01}(\tilde{s}_{(i,j,t)} + \frac{\tau}{\delta^2} d_{21} \nabla_d^2 \tilde{a}_{(i,j,t)} + \frac{\tau}{\delta^2} d_{22} \nabla_d^2 \tilde{s}_{(i,j,t)}) + O(2), \qquad (3.21b)\end{aligned}$$

if the disturbance is minor, and $O(2)$ represents a polynomial term in the variables (w, z, τ) of the order equal to or great than 2.

Taking the eigenvector X_{kl}^{ij} corresponding to the eigenvalue λ_{kl} and multiplying it with both sides of equation (3.21) gives:

$$\begin{aligned}X_{kl}^{ij} \tilde{a}_{(i,j,t+1)} =& a_{100} X_{kl}^{ij} \tilde{a}_{(i,j,t)} + a_{010} X_{kl}^{ij} \tilde{s}_{(i,j,t)} + \frac{\tau}{\delta^2}\big(a_{100} d_{11} + a_{010} d_{21}\big) X_{kl}^{ij} \nabla_d^2 \tilde{a}_{(i,j,t)} \\ &+ \frac{\tau}{\delta^2}\big(a_{100} d_{12} + a_{010} d_{22}\big) X_{kl}^{ij} \nabla_d^2 \tilde{s}_{(i,j,t)}, \qquad (3.22a)\\ X_{kl}^{ij} \tilde{s}_{(i,j,t+1)} =& b_{100} X_{kl}^{ij} \tilde{a}_{(i,j,t)} + b_{010} X_{kl}^{ij} \tilde{s}_{(i,j,t)} + \frac{\tau}{\delta^2}\big(b_{100} d_{11} + b_{010} d_{21}\big) X_{kl}^{ij} \nabla_d^2 \tilde{a}_{(i,j,t)}\end{aligned}$$

$$+\frac{\tau}{\delta^2}\big(b_{100}d_{12}+b_{010}d_{22}\big)X_{kl}^{ij}\nabla_d^2\tilde{s}_{(i,j,t)}. \tag{3.22b}$$

Taking the sum over all i and j on both sides of equation (3.22) yields:

$$\begin{aligned}\sum_{i,j=1}^{n}X_{kl}^{ij}\tilde{a}_{(i,j,t+1)}=&a_{100}\sum_{i,j=1}^{n}X_{kl}^{ij}\tilde{a}_{(i,j,t)}+a_{010}\sum_{i,j=1}^{n}X_{kl}^{ij}\tilde{s}_{(i,j,t)}+\frac{\tau}{\delta^2}\big(a_{100}d_{11}+a_{010}d_{21}\big)\\&\times\sum_{i,j=1}^{n}X_{kl}^{ij}\nabla_d^2\tilde{a}_{(i,j,t)}+\frac{\tau}{\delta^2}\big(a_{100}d_{12}+a_{010}d_{22}\big)\sum_{i,j=1}^{n}X_{kl}^{ij}\nabla_d^2\tilde{s}_{(i,j,t)},\end{aligned} \tag{3.23a}$$

$$\begin{aligned}\sum_{i,j=1}^{n}X_{kl}^{ij}\tilde{s}_{(i,j,t+1)}=&b_{100}\sum_{i,j=1}^{n}X_{kl}^{ij}\tilde{a}_{(i,j,t)}+b_{010}\sum_{i,j=1}^{n}X_{kl}^{ij}\tilde{s}_{(i,j,t)}+\frac{\tau}{\delta^2}\big(b_{100}d_{11}+b_{010}d_{21}\big)\\&\times\sum_{i,j=1}^{n}X_{kl}^{ij}\nabla_d^2\tilde{a}_{(i,j,t)}+\frac{\tau}{\delta^2}\big(b_{100}d_{12}+b_{010}d_{22}\big)\sum_{i,j=1}^{n}X_{kl}^{ij}\nabla_d^2\tilde{s}_{(i,j,t)}.\end{aligned} \tag{3.23b}$$

Let $\overline{a}_t=\sum X_{kl}^{ij}\tilde{a}_{(i,j,t)}, \overline{s}_t=\sum X_{kl}^{ij}\tilde{s}_{(i,j,t)}$, then system (3.23) can be transformed into the following form:

$$\overline{a}_{t+1}=A_{11}\overline{a}_t+A_{12}\overline{s}_t, \tag{3.24a}$$

$$\overline{s}_{t+1}=A_{21}\overline{a}_t+A_{22}\overline{s}_t, \tag{3.24b}$$

where

$$\begin{aligned}A_{11}&=a_{100}-\frac{\tau}{\delta^2}\left(a_{100}d_{11}+a_{010}d_{21}\right)\lambda_{kl},\ A_{12}=a_{010}-\frac{\tau}{\delta^2}\left(a_{100}d_{12}+a_{010}d_{22}\right)\lambda_{kl},\\A_{21}&=b_{100}-\frac{\tau}{\delta^2}\left(b_{100}d_{11}+b_{010}d_{21}\right)\lambda_{kl},\ A_{22}=b_{010}-\frac{\tau}{\delta^2}\left(b_{100}d_{12}+b_{010}d_{22}\right)\lambda_{kl}.\end{aligned}$$

The dynamic behavior of spatial inhomogeneous disturbance solutions are depicted by system (3.24). When the system of equations diverges, the discrete system will undergo spatial symmetry breaking at (a_*,s_*), leading to the formation of Turing patterns. It is clear that the divergence of the discrete system of equations is directly linked to the two eigenvalues:

$$\lambda_\pm(k,l)=\frac{1}{2}\bigg(\big(A_{11}+A_{22}\big)\pm\sqrt{\big(A_{11}+A_{22}\big)^2-4A_{12}A_{21}}\bigg), \tag{3.25}$$

when $|\lambda_+(k,l)|>1$ or $|\lambda_-(k,l)|>1$, the fixed point $(0,0)$ of system (3.24) is unstable, which indicates the homogeneous steady state (a_*,s_*) becomes unstable.

Moreover, denote

$$Z(k,l,\tau)=\max\left\{|\lambda_+(k,l)|,|\lambda_-(k,l)|\right\}, \tag{3.26}$$

$$Z_m(\tau)=\max_{k=1}^{n}\max_{l=1}^{n}Z(k,l,\tau),\ (k,l)\neq(1,1). \tag{3.27}$$

The threshold condition for Turing bifurcation is $Z_m(\tau')=1$, and the critical value τ' can be described by the following proposition.

Proposition 3.1. *(1) When τ is close to τ', if $(A_{11}(k,l,\tau')+A_{22}(k,l,\tau'))^2>4A_{12}(k,l,\tau')A_{21}(k,l,\tau')$ is satisfied, then critical value τ' can be attained by $\max\limits_{k=1,l=1}^{n}\big(\big|A_{11}(k,l,\tau')+A_{22}(k,l,\tau')\big|-A_{12}(k,l,\tau')A_{21}(k,l,\tau')\big)=1$.*
(2) If $(A_{11}(k,l,\tau')+A_{22}(k,l,\tau'))^2\le 4A_{12}(k,l,\tau')A_{21}(k,l,\tau')$ when τ is close to τ', then critical value τ' can be attained by $\max\limits_{k=1,l=1}^{n}A_{12}(k,l,\tau')A_{21}(k,l,\tau')=1$.

Based on the above analysis, we have the following theorems.

Theorem 3.3. *Under the assumption that one of* (SN_1)-(SN_2), (H_3)–(H_4) *and* (SF_1)-(SF_2) *is valid and* τ *is close to* τ', *if* $Z_m(\tau) > 1$, *then the homogeneous steady state* (a_*, s_*) *of CMLs model (2.1)-(2.4) with periodic conditions is subject to Turing instability, leading to the emergence of Turing patterns. Conversely, if* $Z_m(\tau) < 1$, *the homogeneous steady state* (a_*, s_*) *of CMLs model remains stable, and no Turing patterns will arise.*

4. Numerical simulation

In this section, we will present several illustrative examples to demonstrate the dynamic evolution of flip, Neimark–Sacker bifurcations, and Turing instability, along with their corresponding spatiotemporal patterns.

4.1. The dynamics behaviors for spatially homogeneous state

Firstly, we will demonstrate the temporal dynamics of Flip bifurcation and Neimark-Sacker bifurcation in this subsection. We set $\sigma = 0.6$, and $\mu = 2$, thus the only positive equilibrium point is $(a_*, s_*) = (1.6, 0.390625)$, and the critical value for flip bifurcation is $\tau_1 = 0.599778$. Taking $\tau = \tau_1$, then the eigenvalues are -1 and 0.07908. Based on the calculations, we have determined that $\eta_1 = -3.7015 < 0$, and $\eta_2 = 1.0995 > 0$. According to Theorem 3.1, the period-2 orbit that undergoes bifurcation is stable when τ is in the right neighborhood of τ_1. We plot the corresponding bifurcation diagram, please refer to Fig. 3(a). From 3(a) we can clearly observe the period-doubling cascade of the activator a. And When $\sigma = 0.8$, and $\mu = 0.2$, then the only positive equilibrium point is $(a_*, s_*) = (1.8, 0.308642)$, and the critical value for Neimark-Sacker bifurcation is $\tau_* = 0.828532$. After further calculation, we get the eigenvalues of the corresponding Jacobian matrix are 0.777585 ± 0.628778, which the the modules are both 1. And the discriminatory quantity $\kappa = -0.095 < 0$, $d = 0.2684 > 0$, so according to Theorem 3.2, the Neimark-Sacker occurs and an attracting invariant cycle will appear for $\tau > \tau_*$. The Neimark-Sacker bifurcation diagram are shown in Figure 3(b).

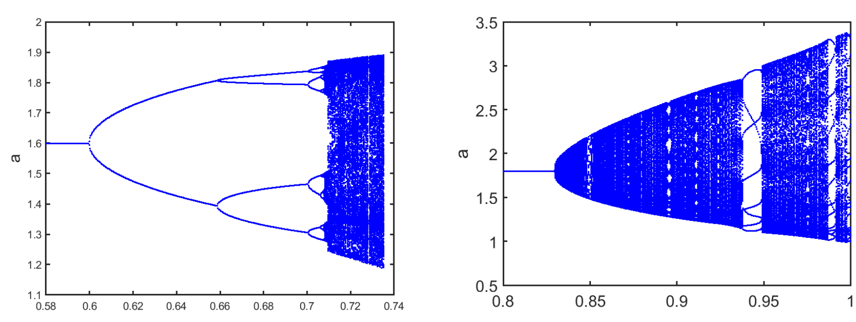

Figure 3. (a) Flip bifurcation diagram; (b) Neimark-Sacker bifurcation diagram.

Next, we provide the corresponding maximum Lyapunov exponents for flip bifurcation and Neimark-Sacker bifurcation, which can quantitatively determine the chaotic and non-chaotic behaviors, as shown in Figure 4(a) and Figure 4(b), respectively.

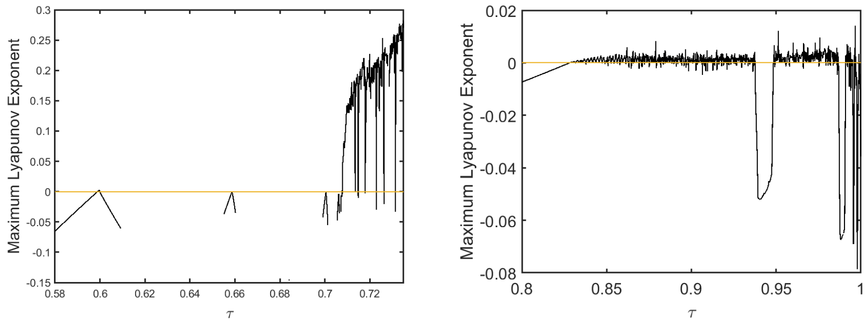

Figure 4. (a) Maximum Lyapunov exponents of Flip bifurcation; (b) Maximum Lyapunov exponents of Neimark-Sacker bifurcation.

Besides, the phase orbits for flip bifurcation and Neimark–Sacker bifurcation are presented in Figures 5 and 6, respectively. From Figure 5, we can see that as the value of τ slowly increases, when τ is greater than τ_1, there exists stable period–2, 4, 8, 10 point, as shown in Figures 5(a)-(c), (f), respectively. A complex periodic orbit is shown in 5(d). When τ increases to a certain extent, we can observe the emergence of chaotic phenomena, which is specifically shown in Figure 5(e). From the observation of Figure 6, it can be seen that when $\tau = 0.826 < \tau_*$, Figure 6(a) shows a stable fixed point. For $\tau = 0.86 > \tau_*$, Figure 6(b) exhibits a stable invariant circle. And 6(c) shows a quasi periodic orbit for $\tau = 0.937$. Figure 6(d) and 6(e) display the period-8 window and period-15 window, respectively, corresponding to $\tau = 0.948$ and $\tau = 0.99$. And we can also find chaos (Figure 6(f)) as τ increases furthermore.

4.2. The dynamics behaviors for spatially heterogenous state

In this section, we present the spatiotemporal dynamics of Turing instability for flip bifurcation and Neimark–Sacker bifurcation. In order to guarantee the formation of the pattern, we must confirm $\frac{\max\{d_{11},d_{12},d_{21},d_{22}\}\tau}{\delta^2} < 0.5$ according to [3].

Let $d_{11} = 0.5$, $d_{12} = 0$, $d_{21} = 0$, $d_{22} = 0.6$ and $\delta = 10$, the $Z_m - \tau$ diagrams are shown in 7(a). By utilizing the provided parametric values, we determine the critical value for the Turing bifurcation $\tau' \approx 0.5998$. Through the combination of the flip bifurcation curve $\tau = \tau_1$ and the Turing bifurcation curve $\tau = \tau'$, we illustrate the regions where pattern formation takes place in Figure 7(b), with d_{22} varying from 0 to 40. Three regions are gained: homogeneous stationary state region, pure-Turing instability region, and flip-Turing instability region.

Moreover, we set $d_{11} = 0.5$, $d_{12} = 0$, $d_{21} = 0$, $d_{22} = 0.8$ and $\delta = 6$, the $Z_m - \tau$ diagrams are presented in 8(a). In the same vein, we can ascertain the critical value for the Turing bifurcation $\tau' \approx 0.82838$. In this case, the Turing bifurcation curve $\tau = \tau'$ and the Neimark-Sacker bifurcation curve $\tau = \tau_*$ also partition parametric space, (d_{22}, τ) into three distinct regions, namely: homogeneous stationary state region, pure-Turing instability region, and Neimark-Sacker-Turing instability region, as depicted in Figure 8(b).

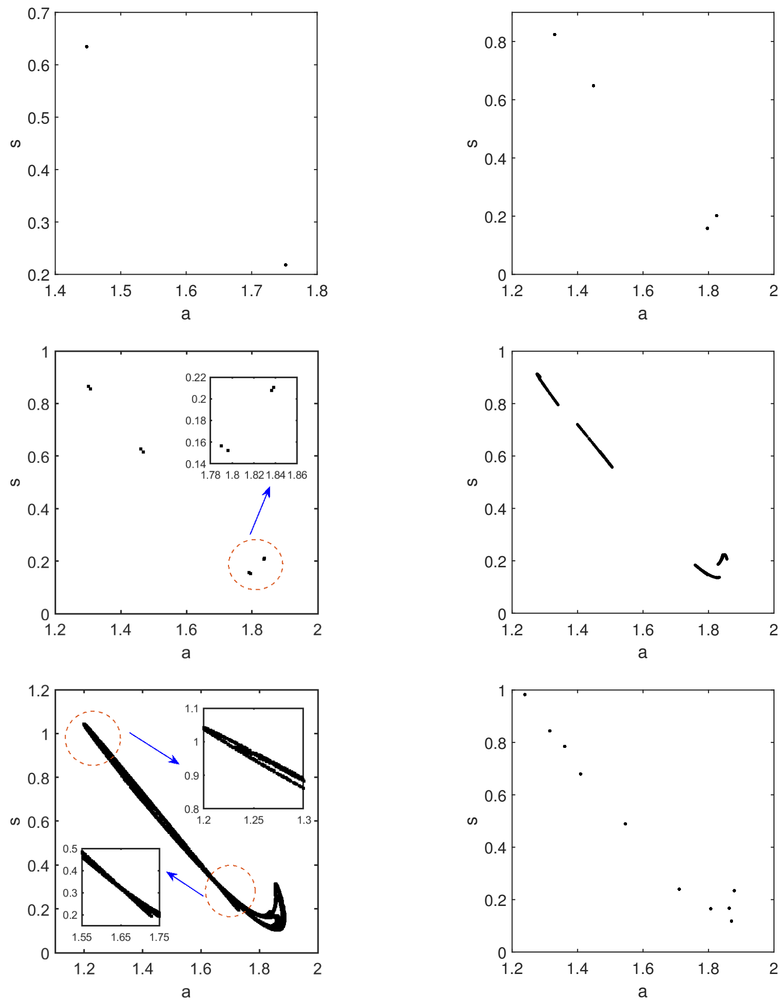

Figure 5. Phase portraits for different values of τ corresponding to Figure 3(a). (a) $\tau = 0.63$; (b) $\tau = 0.68$; (c) $\tau = 0.7006$; (d) $\tau = 0.7093$; (e) $\tau = 0.73$; (f) $\tau = 0.736$.

In the subsequent sections, we will showcase the patterns that arise from the flip-Turing instability and Neimark-Sacker-Turing instability, respectively. And the spatial patterns depicted in all the figures represent the spatial distribution of the CMLs model at t=20,000. The initial state is a random perturbation applied to the homogeneous stationary state (a_*, s_*).

Firstly, we analyze the Turing patterns induced by the flip-Turing instability with self-diffusion. Set $d_{11} = 0.5$, $d_{12} = 0$, $d_{21} = 0$, $d_{22} = 0.6$, $\delta = 10$, and $n = 100$. When $\tau = 0.56$, there will be no occurrence of either Turing bifurcation or flip bifurcation, and the stable homogeneous stationary state remains locally uniformly stable. Consequently, spatial patterns will not emerge, please see Figure 9(a). For $\tau = 0.602$, the Turing bifurcation and flip bifurcation occur concurrently in the CMLs model (2.1)-(2.4). At this moment, spatially heterogeneous patterns will emerge in the CMLs model due to the flip-Turing instability mechanism, please

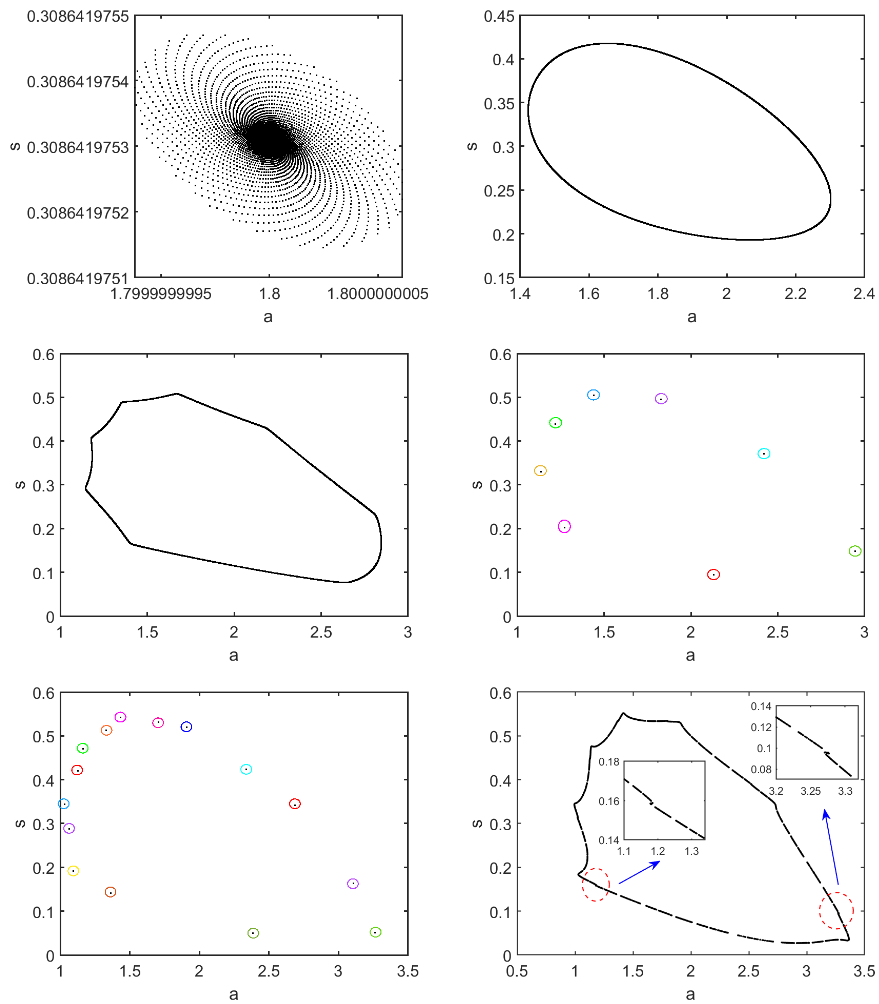

Figure 6. Phase portraits for different values of τ corresponding to Figure 3(b). (a) $\tau = 0.826$; (b) $\tau = 0.86$; (c) $\tau = 0.937$; (d) $\tau = 0.948$; (e) $\tau = 0.99$; (f) $\tau = 0.9962$.

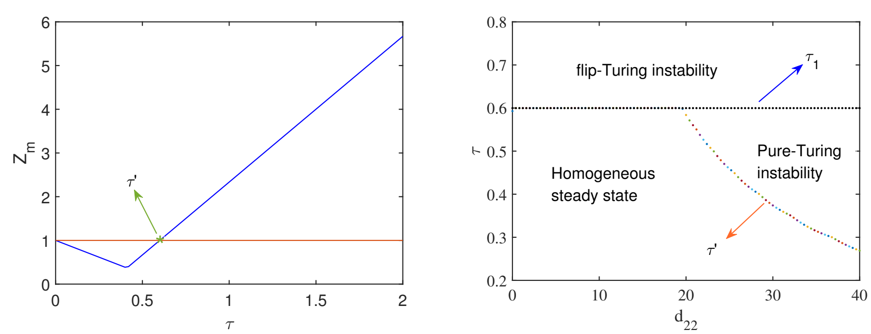

Figure 7. (a) $Z_m - \tau$ diagram showing the Turing bifurcation; (b) $\tau - d_{22}$ diagram showing pattern formation region.

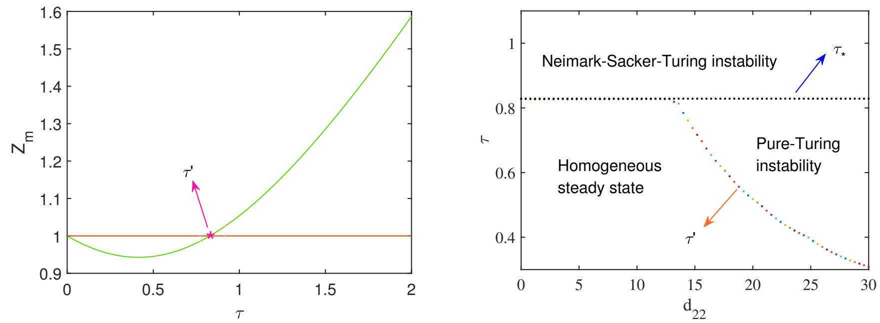

Figure 8. (a) $Z_m - \tau$ graph showing the Turing bifurcation; (b) $\tau - d_{22}$ graph showing the regions for spatial patterns formation.

consult Figure 9(b) for reference, which are formed by two alteration states, namely, the period-2 points. Similarly, with $\tau = 0.68$, we can visualize the patterns induced by the period-4 points, as displayed in Figure 9(c). Taking $\tau = 0.7006$, we observe a spatial pattern inlaying with eight states (Figure 9(d)), which is dominated by period-8 points. When τ is set to $\tau = 0.7093$, we notice patterns that are characterized by increased fragmentation, as illustrated in Figure 9(e). With $\tau = 0.73$, we can observe from Figure 9(e) that the dynamics of the CMLs model exhibit chaotic behavior. Meanwhile, the associated patterns also exhibit chaotic characteristics. The pattern takes on a mosaic-like appearance, making it difficult to determine the number of colors present, as shown in Figure 9(f). As τ increases further, at $\tau = 0.736$, we observe the presence of patterns induced by period-10 points, please refer to Figure 9(g).

Next, we discuss the influence of cross-diffusion on the pattern formation. Set $d_{12} = 0.05$ and $d_{21} = 0.06$, and other parameters are given the same as in Figure 9. The corresponding patterns are shown in Figure 10 for different τ. By comparing Figure 10 with Figure 9, we observe that the patterns in Figure 10 resemble those in Figure 9. For instance, patterns in Figs. 9(a) and 10(a) are both in a homogeneous steady state, which are triggered by the periodic-2 points and are formed through repeated alternation of two states. Furthermore, the patterns in Figs. 9(e) and 10(e) are induced by chaotic attractors and break into fragments. Additionally, we find that the sizes of plaques in Figure 10 differ from those in Figure 9, as seen in the patterns of Figs. 9(b) and 10(b). It appears that cross-diffusion may have an impact on the size of patterns.

In the following, we investigate the patterns induced by the Neimark-Sacker-Turing instability with self-diffusion. Set $d_{11} = 0.5$, $d_{12} = 0$, $d_{21} = 0$, $d_{22} = 0.8$, $\delta = 10$, and $n = 100$. When $\tau = 0.826$, that is $\tau < \tau'$. Currently, there will be no occurrence of either Neimark-Sacker bifurcation or Turing bifurcation. Therefore, no pattern will be generated, as shown in Figure 11(a). When $\tau > \tau_*$, the CMLs model undergoes Neimark–Sacker–Turing instability at this moment and leads to spatial heterogeneous patterns. In particular, when $\tau = 0.86$, the pattern induced by invariant circles, be shown in Figure 11(b). As τ increases to 0.937, we can observe that the patterns generated in Figure 11(c), become increasingly distorted. And when τ is 0.948, the pattern induced by the periodic-8 orbit is depicted in Figure 11(d). Compared to the situation when $\tau = 0.937$, these patterns have become more clustered and dense. Continuing to vary the value of τ, when $\tau = 0.99$, we

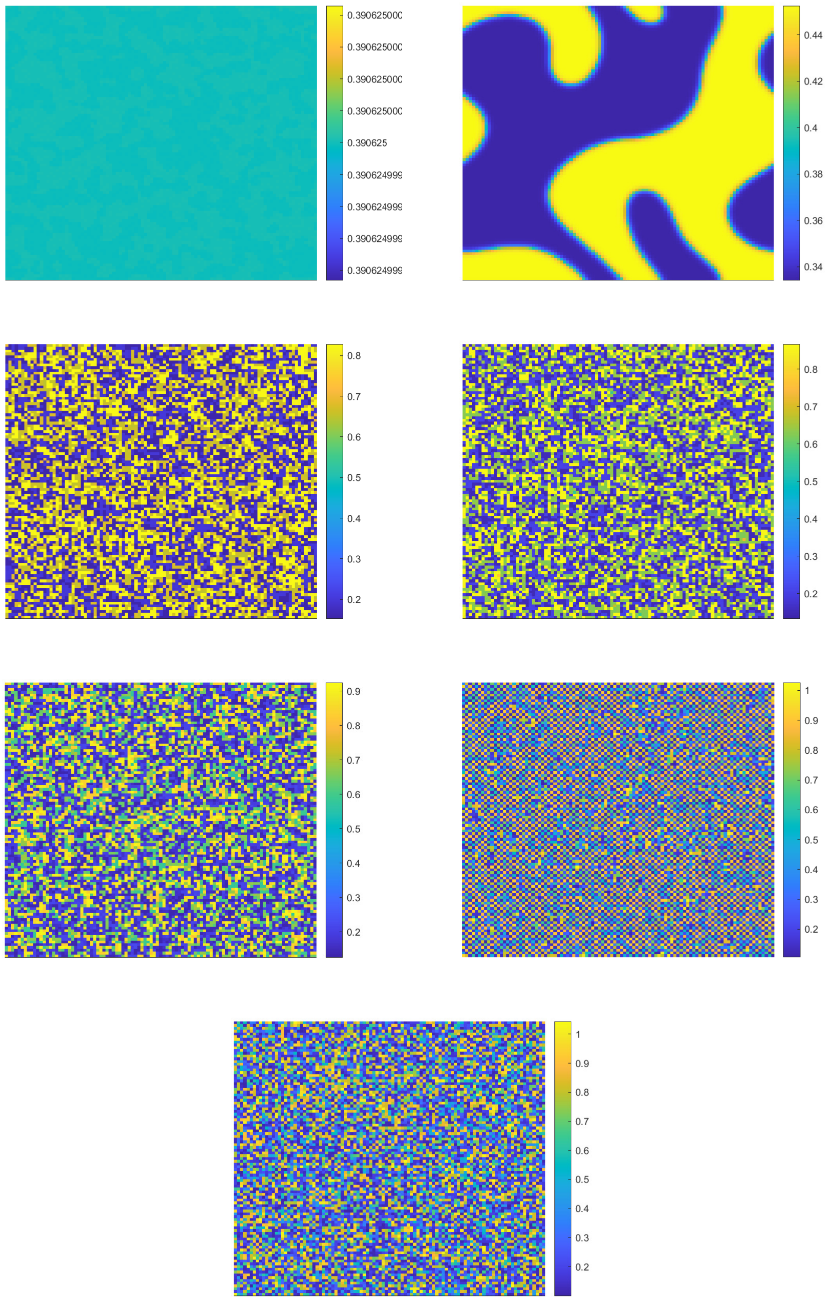

Figure 9. Spatial patterns induced by flip-Turing instability with $d_{11} = 0.5$, $d_{12} = 0$, $d_{21} = 0$, $d_{22} = 0.6$ in different values of τ. (a) $\tau = 0.56$; (b) $\tau = 0.602$; (c) $\tau = 0.68$; (d) $\tau = 0.7006$; (e) $\tau = 0.7093$; (f) $\tau = 0.73$; (g) $\tau = 0.736$.

can observe the emergence of spiral patterns induced by the period-15 points, as shown in Figure 11(e). And when τ is 0.9962, we can see that the patterns generated

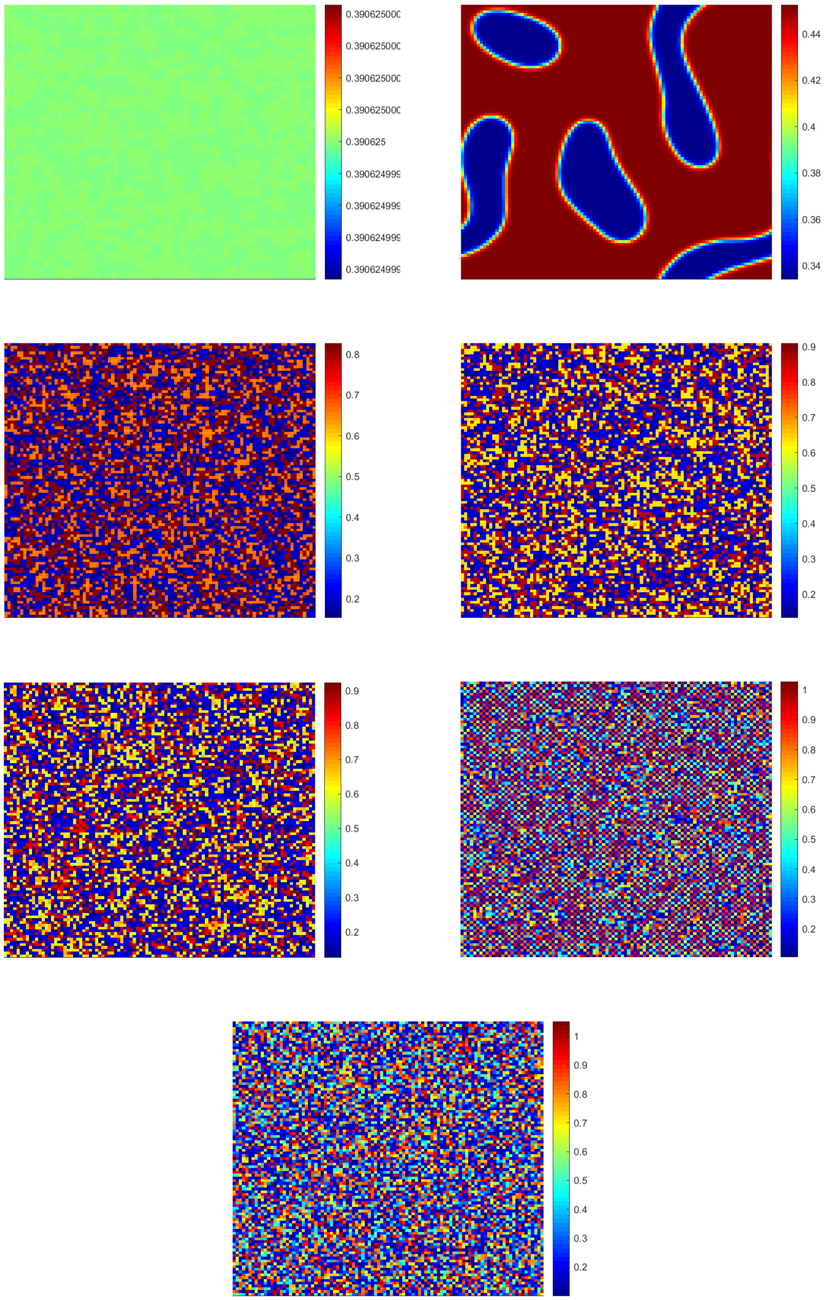

Figure 10. Spatial patterns induced by flip-Turing instability with $d_{11} = 0.5$, $d_{12} = 0.05$, $d_{21} = 0.06$, $d_{22} = 0.6$ in different values of τ. (a) $\tau = 0.56$; (b) $\tau = 0.602$; (c) $\tau = 0.68$; (d) $\tau = 0.7006$; (e) $\tau = 0.7093$; (f) $\tau = 0.73$; (g) $\tau = 0.736$.

at this moment in Figure 11(f) are more disordered and chaotic than Figure 11(e). The reason for this phenomenon is that the patterns are induced by uniform chaotic oscillations.

Finally, the effect of cross-diffusion on pattern formation is considered. Taking $d_{12} = 0.1$ and $d_{21} = 0.05$, and other parameters are given the same as in Figure 11. The corresponding patterns are illustrated in Figure 12 for various values of τ. By comparing Figs. 12 with 11, we can observe that the Turing patterns in Figure 12 share similarities with those in Figure 11, but their sizes are significantly different from those in Figure 11. Additionally, as cross-diffusion coefficients increase, particularly when $d_{12} = 0.5$ and $d_{21} = 0.25$, the patterns shown in Figure 13 emerge for distinct values of τ. Comparing Figure 11 with Figure 13, we notice that the patterns in Figs. 13(c)-(e) take on a curled shape, while those in Figs. 11(c)-(e) appear as circles. This suggests that cross-diffusion has an impact on both the size and type of pattern formation.

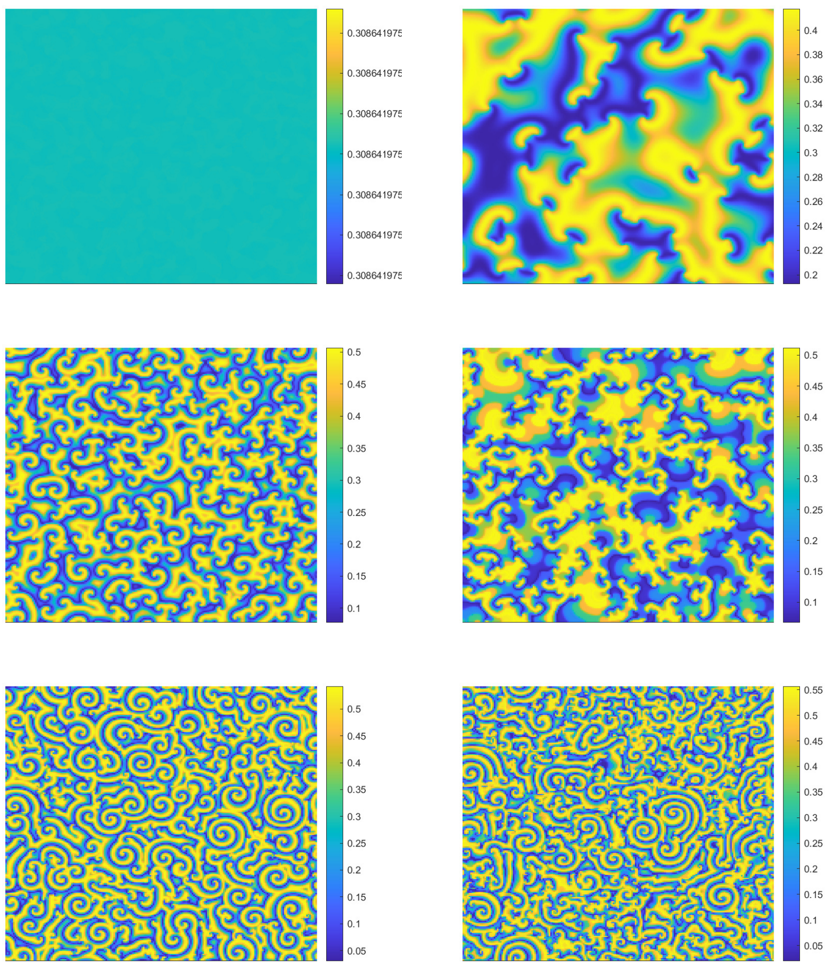

Figure 11. Spatial patterns induced by Neimark-Sacker-Turing instability with $d_{11} = 0.5$, $d_{12} = 0$, $d_{21} = 0$, $d_{22} = 0.8$ in different values of τ. (a) $\tau = 0.826$; (b) $\tau = 0.86$; (c) $\tau = 0.937$; (d) $\tau = 0.948$; (e) $\tau = 0.99$; (f) $\tau = 0.9962$.

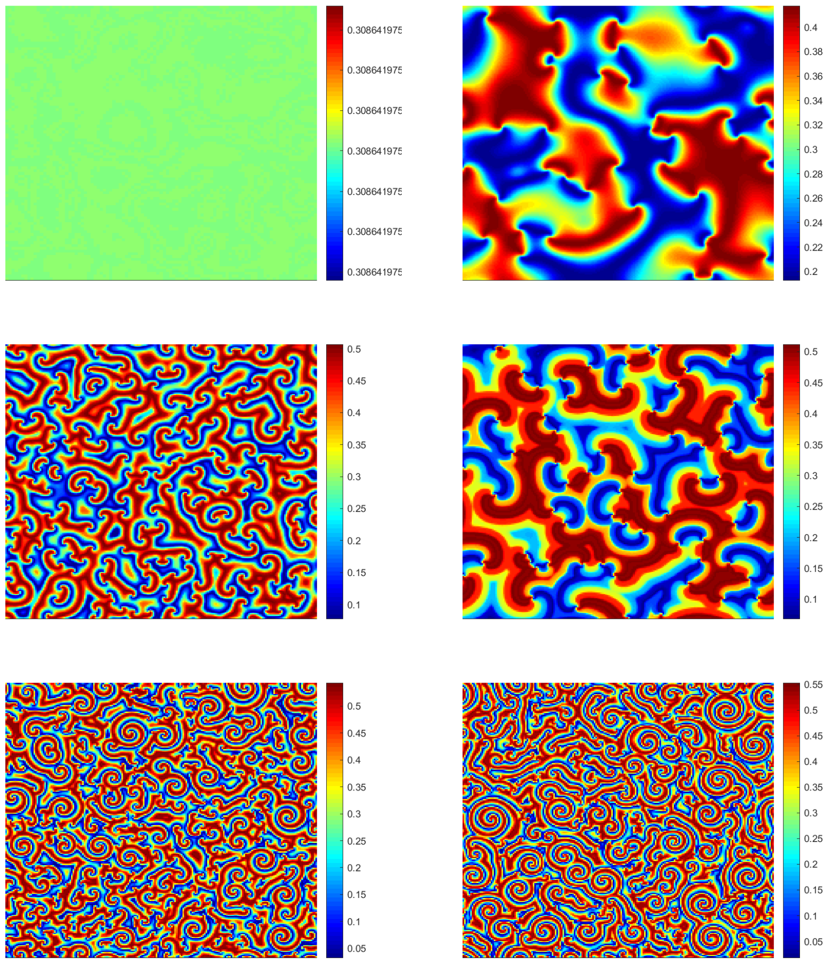

Figure 12. Spatial patterns induced by Neimark-Sacker-Turing instability with $d_{11} = 0.5$, $d_{12} = 0.1$, $d_{21} = 0.05$, $d_{22} = 0.8$ in different values of τ. (a) $\tau = 0.826$; (b) $\tau = 0.86$; (c) $\tau = 0.937$; (d) $\tau = 0.948$; (e) $\tau = 0.99$; (f) $\tau = 0.9962$.

Remark 4.1. In [14], Gu et al. studied the stability of equilibrium point, Hopf bifurcation and Turing bifurcation for the continuous reaction-diffusion equation, and obtained the spot and stripe patterns by numerical simulation. In this paper, the reaction-diffusion equation of spatiotemporal discretization, that is, the corresponding CMLs model (2.1)–(2.4) is studied. Compared with the results obtained in [14], firstly, the continuous system and the CMLs model have the same equilibrium point, and the existence conditions of the type of equilibrium point (stable node and stable focus) of the two are the same in the sense of parameter μ and parameter σ, while the type of equilibrium point of the CMLs model is also related to τ. Secondly, both the continuous model and CMLs model have Hopf bifurcation (or Neimark-Sacker bifurcation). The Hopf bifurcation of the continuous system are supercritical, that is, the variable that determines the direction of the Hopf bifurcation $\sigma' < 0$. However, the variable κ for determining the direction of the invariant

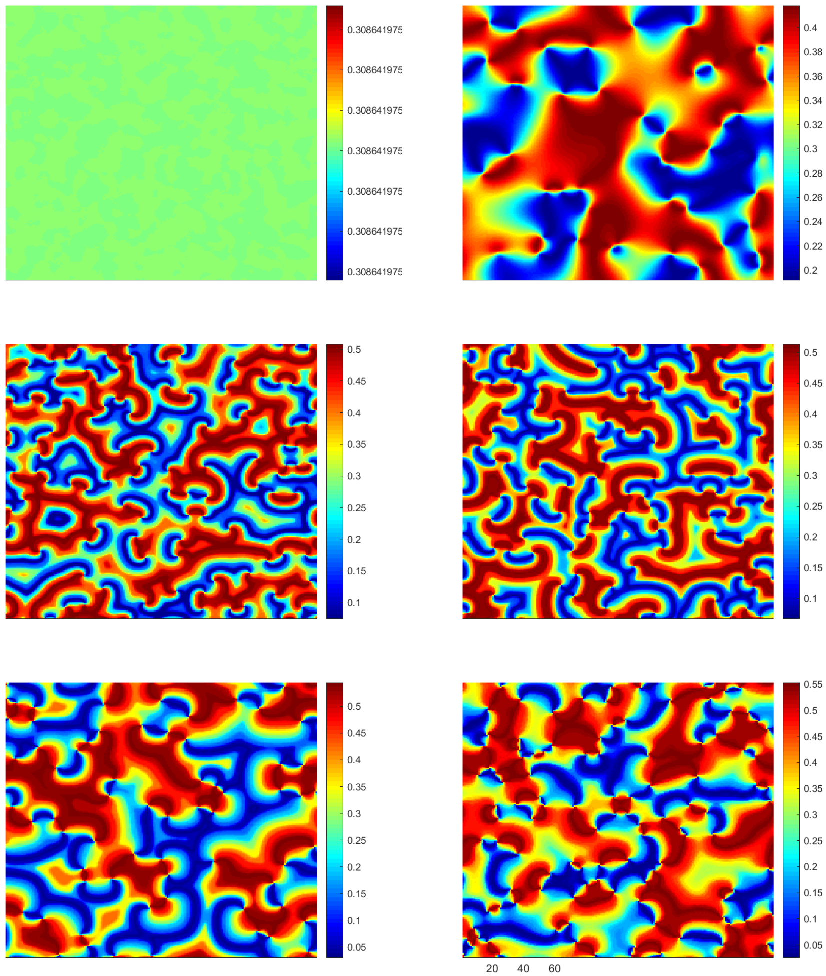

Figure 13. Spatial patterns induced by Neimark-Sacker-Turing instability with $d_{11} = 0.5$, $d_{12} = 0.5$, $d_{21} = 0.25$, $d_{22} = 0.8$ in different values of τ. (a) $\tau = 0.826$; (b) $\tau = 0.86$; (c) $\tau = 0.937$; (d) $\tau = 0.948$; (e) $\tau = 0.99$; (f) $\tau = 0.9962$.

circle of the Hopf bifurcation studied in this paper can be greater than or less than 0. Finally, both the continuous model and the CMLs have Turing bifurcation. The patterns generated by the Turing instability of the continuous system are either spot or stripe, while the Turing patterns generated by the CMLs have many types, including plaques, mosaics, curls, spirals and so on. Therefore, the CMLs model produces a richer patterns than the original continuous system.

5. Conclusions and discussions

This paper explores the spatiotemporal dynamics of a space-time discrete depletion type G-M model with self-diffusion and cross-diffusion. Initially, the CMLs model for the depletion type G-M model with self-diffusion and cross-diffusion are constructed. Subsequently, we focus on analyzing the spatial homogeneous dynamics of CMLs model and derive the conditions for the existence and stability of fixed points, as well as critical parameter values for the occurrence of bifurcations. Through the numerical simulations of spatial homogeneous dynamics, we discover that CMLs model can display intricate dynamical behaviors, including period-doubling cascades, invariant circles, periodic windows, chaotic regions, and more.

In the following, we employ the methods outlined in [20, 21] to investigate the spatial heterogeneous dynamics of CMLs models. Due to the existence of two curves, Turing bifurcation curve and flip (or Neimark-Sacker) bifurcation curve, the parameter space (d_{22}, τ) of depletion type G-M model can be divided into three regions, which are called homogenous steady state region, pure Turing instability region, and flip–Turing (or Neimark-Sacker-Turing) instability region, respectively. We focus on the pattern formation in both the flip-Turing and Neimark–Sacker–Turing instability regions. Through our analysis, we find that there does exist Turing instability in space-time discrete depletion type G-M model with self-diffusion as time scale τ varies. And the emergence of intriguing patterns, including plaques, curls, and spirals are identified, which are not observed in their continuous counterparts. In addition, we examine the role of cross-diffusion in pattern formation by conducting numerical simulations and find that it significantly influences the size and type of patterns. The variation in the sizes and type of patterns may suggest that changes in cross-diffusion have an effect on pigmentation patterns in sea shells and the ontogeny of ribbing on ammonoid shells.

It is worth emphasizing that the fixed point can undergo other bifurcation types, such as saddle-node bifurcation. Exploring these bifurcation types will be the focus of our future research. In addition, the coupled map lattice model is a type of nonlinear dynamical model that combines discrete time and space variables with continuous variables. It includes various discretization forms, such as equilateral triangular neighborhood structure, von Neumann neighborhood structure, pentagonal neighborhood structure, and Moore neighborhood structure. Hence, our future research will also consider the formation of patterns in the system under multiple representative neighborhood structures.

References

[1] W. Abid, R. Yafia, M. A. Aziz-Alaoui, H. Bouhafa and A. Abichou, *Diffusion driven instability and Hopf bifurcation in spatial predator-prey model on a circular domain*, Applied Mathematics and Computation, 2015, 260, 292–313.

[2] L. Bai and G. Zhang, *Nontrivial solutions for a nonlinear discrete elliptic equation with periodic boundary conditions*, Applied Mathematics and Computation, 2009, 210(2), 321–333.

[3] M. Banerjee, *Comments on "L. N. Guin, M. Haque and P. K. Mandal, The spatial patterns through diffusion-driven instability in a predator-prey model, Applied Mathematical Modelling, 2012, 36, 1825-1841."*, Applied Mathematical Modelling, 2015, 39(1), 297–299.

[4] M. Bendahmane, R. Ruiz-Baier and C. Tian, *Turing pattern dynamics and adaptive discretization for a super-diffusive Lotka-Volterra model*, Journal of Mathematical Biology, 2016, 72(6), 1441–1465.

[5] J. Buceta and K. Lindenberg, *Switching-induced Turing instability*, Physical Review E, 2002, 66(4), 046202.

[6] Y. Cai, C. Zhao and W. Wang, *Spatiotemporal complexity of a Leslie-Gower predator-prey model with the weak Allee effect*, Journal of Applied Mathematics, 2013. DOI: 10.1155/2013/535746.

[7] C. Castellano, S. Fortunato and V. Loreto, *Statistical physics of social dynamics*, Reviews of Modern Physics, 2007, 81(2), 591–646.

[8] C. Castellano, H. Zhang and L. Dai, *Regular and irregular vegetation pattern formation in semiarid regions: A study on discrete klausmeier model*, Complexity, 2020, 2020, 2498073.

[9] L. Chang, G. Sun, Z. Wang and Z. Jin, *Rich dynamics in a spatial predator-prey model with delay*, Applied Mathematics and Computation, 2015, 256, 540–550.

[10] M. Chen and Q. Zheng, *Predator-taxis creates spatial pattern of a predator-prey model*, Chaos Solitons & Fractals, 2022, 161, 112332.

[11] G. Domokos and I. Scheuring, *Discrete and continuous state population models in a noisy world*, Journal of Theoretical Biology, 2004, 227(4), 535–545.

[12] S. Getzin, T. E. Erickson, H. Yizhaq, M. Muñoz-Rojas, A. Huth and K. Wiegand, *Bridging ecology and physics: Australian fairy circles regenerate following model assumptions on ecohydrological feedbacks*, Journal of Ecology, 2021, 109(1), 399–416.

[13] A. Gierer and H. Meinhardt, *Stripe and spot patterns in a gierer-meinhardt activator-inhibitor model with different sources*, Kybernetik, 1972, 12(1), 30–39.

[14] L. Gu, P. Gong and H. Wang, *Bifurcation and Turing instability analysis for the Gierer-Meinhardt model of the depletion type*, Discrete Dynamics in Nature and Society, 2020, 2020, 5293748.

[15] J. Guckenheimer and P. Holms, *Nonlinear Oscillations, Dynamical Systems, and Bifurcations of Vector Fields*, Springer, New York, 1983.

[16] O. Hammer and H. Bucher, *Reaction-diffusion processes: Application to the morphogenesis of ammonoid ornamentation*, Physical Review E, 1999, 32(6), 841–852.

[17] R. Han and B. Dai, *Spatiotemporal pattern formation and selection induced by nonlinear cross-diffusion in a toxic-phytoplankton-zooplankton model with Allee effect*, Nonlinear Analysis-Real World Applications, 2019, 45, 822–853.

[18] R. Han, L. N. Guin and B. Dai, *Cross-diffusion-driven pattern formation and selection in a modified Leslie-Gower predator-prey model with fear effect*, Journal of Biological Systems, 2020, 28(1), 27–64.

[19] H. He, M. Xiao, J. He and W. Zheng, *Regulating spatiotemporal dynamics for a delay Gierer-Meinhardt model*, Physica A-Statistical Mechanics and its Applications, 2024, 637, 129603.

[20] T. Huang and H. Zhang, *Bifurcation, chaos and pattern formation in a space- and time-discrete predator-prey system*, Chaos Solitons & Fractals, 2016, 91, 92–107.

[21] T. Huang, H. Zhang and H. Yang, *Spatiotemporal complexity of a discrete space-time predator-prey system with self- and cross-diffusion*, Applied Mathematicak Modelling, 2017, 47, 637–655.

[22] Z. Jing and J. Yang, *Bifurcation and chaos in discrete-time predator-prey system*, Chaos Solitons & Fractals, 2006, 27(1), 259–277.

[23] Y. Li, J. Wang and X. Hou, *Stripe and spot patterns for the Gierer-Meinhardt model with saturated activator production*, Journal of Mathematical Analysis and Applications, 2017, 449(2), 1863–1879.

[24] B. Liu, R. Wu and L. Chen, *Turing-Hopf bifurcation analysis in a superdiffusive predator-prey model*, Chaos, 2018, 28(11), 1–10.

[25] B. Liu, R. Wu, N. Iqbal and L. Chen, *Turing patterns in the Lengyel-Epstein system with superdiffusion*, International Journal of Bifurcation and Chaos, 2017, 27(8), 1–17.

[26] J. Liu, F. Yi and J. Wei, *Multiple bifurcation analysis and spatiotemporal patterns in a 1-D Gierer-Meinhardt model of morphogenesis*, International Journal of Bifurcation and Chaos, 2010, 20(4), 1007–1025.

[27] X. Liu and D. Xiao, *Complex dynamic behaviors of a discrete-time predator-prey system*, Chaos Solitons & Fractals, 2007, 32(1), 80–94.

[28] F. Mai, L. Qin and G. Zhang, *Turing instability for a semi-discrete Gierer-Meinhardt system*, Physica A-Statistical Mechanics and Its Applications, 2012, 391(5), 2014–2022.

[29] H. Meinhardt and M. Klingler, *A model for pattern formation on the shells of molluscs*, Journal of Theoretical Biology, 1987, 126(1), 63–89.

[30] D. Mistro, L. Rodrigues and S. Petrovskii, *Spatiotemporal complexity of biological invasion in a space- and time discrete predator-prey system with strong Allee effect*, Ecological Complexity, 2012, 9, 16–32.

[31] A. Nayfeh and B. Balachandran, *Applied Nonlinear Dynamics: Analytical, Computational, and Experimental Methods*, Wiley, Weinheim, 1995.

[32] K. M. Owolabi and A. Atangana, *Numerical simulation of noninteger order system in subdiffusive, diffusive, and superdiffusive scenarios*, Journal of Computational and Nonlinear Dynamics, 2017, 12(3), 031010.

[33] M. Perc and P. Grigolini, *Collective behavior and evolutionary games-an introduction*, Chaos Solitons & Fractals, 2013, 56, 1–5.

[34] D. Punithan, D. K. Kim and R. I. McKay, *Spatio-temporal dynamics and quantification of daisyworld in two dimensional coupled map lattices*, Ecological Complexity, 2012, 12, 43–57.

[35] L. Rodrigues, D. Mistro and S. Petrovskii, *Pattern formation in a space- and time-discrete predator-prey system with a strong allee effect*, Theoretical Ecology, 2012, 5(3), 341–362.

[36] S. Ruan, *Diffusion–driven instability in the Gierer-Meinhardt model of morphogenesis*, Natural Resource Modeling, 1998, 311(2), 131–141.

[37] X. Tang and Y. Song, *Cross-diffusion induced spatiotemporal patterns in a predator–prey model with herd behavior*, Nonlinear Analysis-Real World Applications, 2015, 24, 36–49.

[38] A. M. Turing, *The chemical basis of morphogenesis*, Bulletin of Mathematical Biology, 1952, 237, 37–72.

[39] H. Wang and P. Liu, *Pattern dynamics of a predator-prey system with cross-diffusion, Allee effect and generalized Holling IV functional response*, Chaos Solitons & Fractals, 2023, 171, 113456.

[40] J. Wang, X. Hou, Y. Li and Z. Jing, *Stripe and spot patterns in a gierer-meinhardt activator-inhibitor model with different sources*, International Journal of Bifurcation and Chaos, 2015, 25(8), 1550108.

[41] J. Wang, Y. Li, S. Zhong and X. Hou, *Analysis of bifurcation, chaos and pattern formation in a discrete time and space Gierer Meinhardt system*, Chaos Solitons & Fractals, 2019, 118, 1–17.

[42] M. J. Ward and J. Wei, *Hopf bifurcations and oscillatory instabilities of spike solutions for the one-dimensional Gierer-Meinhardt model*, Journal of Ninlinear Science, 2003, 13(2), 209–264.

[43] J. Wei and M. Winter, *On the two-dimensional Gierer-Meinhardt system with strong coupling*, SIAM Journal on Mathematical Analysis, 1999, 30(6), 1241–1263.

[44] R. Wu and L. Yang, *Bogdanov-Takens bifurcation of codimension 3 in the Gierer-Meinhardt model*, International Journal of Bifurcation and Chaos, 2023, 33(14), 2350163.

[45] R. Wu, Y. Zhou, Y. Shao and L. Chen, *Bifurcation and Turing patterns of reaction-diffusion activator-inhibitor model*, Physica A-Statistical Mechanics and Its Applications, 2017, 482, 597–610.

[46] R. Yang, *Cross-diffusion induced spatiotemporal patterns in Schnakenberg reaction-diffusion model*, Nonlinear Dynamical, 2020, 110(2), 1753–1766.

[47] R. Yang and X. Yu, *Turing-Hopf bifurcation in diffusive Gierer-Meinhardt model*, International Journal of Bifurcation and Chaos, 2022, 32(05), 2250046.

[48] F. Yi, J. Wei and J. Shi, *Diffusion-driven instability and bifurcation in the Lengyel-Epstein system*, Nonlinear Analysis-Real World Applications, 2008, 9(3), 1038–1051.

[49] Q. Zheng, J. Shen, V. Pandey, L. Guan and Y. Guo, *Turing instability in a network-organized epidemic model with delay*, Chaos Solitons & Fractals, 2023, 168, 113205.

[50] Q. Zheng, J. Shen, Y. Xu, V. Pandey and L. Guan, *Pattern mechanism in stochastic SIR networks with ER connectivity*, Physica A-Statistical Mechanics and its Applications, 2022, 603, 127765.

[51] S. Zhong, J. Wang, J. Bao, Y. Li and N. Jiang, *Spatiotemporal complexity analysis for a space-time discrete generalized toxic phytoplankton-zooplankton model with self-diffusion and cross-diffusion*, International Journal of Bifurcation and Chaos, 2021, 31(1), 2150006.

[52] S. Zhong, J. Wang, Y. Li and N. Jiang, *Bifurcation, chaos and Turing instability analysis for a space-time discrete Toxic Phytoplankton-Zooplankton model with self-diffusion*, International Journal of Bifurcation and Chaos, 2021, 29(13), 1950184.